Characteristics and Dynamics of Density Fronts over the Inner to Mid-shelf under Weak Wind Conditions

XIAODONG WU[1], FALK FEDDERSEN[1], AND SARAH N. GIDDINGS[1]

[1]*Scripps Institution of Oceanography, La Jolla, California, USA*

Revised to *Journal of Physical Oceanography,*

December 2, 2020

Corresponding author address:

X. Wu, Scripps Institution of Oceanography, University of California, San Diego, 9500 Gilman Dr., La Jolla CA 92093-0209

E-mail:x1wu@ucsd.edu

ABSTRACT

Here, we explore the kinematics and dynamics of coastal density fronts (within $10\,\mathrm{km}$ from shore and < 30 m depth), identified using an edge detection algorithm, in a realistic high resolution model of the San Diego Bight with relatively weak winds and small freshwater input. The density fronts have lengths spanning $4 - 10\,\mathrm{km}$ and surface density gradients spanning $2 - 20 \times 10^{-4}\,\mathrm{kg\,m^{-4}}$. Cross-shore oriented fronts are more likely with northward subtidal flow and are 1/3 as numerous as alongshore oriented fronts which are more likely with onshore surface baroclinic diurnal flow. Using a subset of the cross-shore fronts, decomposed into cross-front mean and perturbation components, an ensemble front is created. The ensemble cross-front mean flow is largely geostrophic in the cross- and along-front directions. The ensemble cross-shore front extends several kilometers from shore, with a distinct linear front axis and downwelling (upwelling) on the dense (light) side of the front, convergent perturbation cross-front flow within the upper $5\,\mathrm{m}$, strengthening the ensemble front. Vertical mixing of momentum is weak, counter to the turbulent thermal wind mechanism. The ensemble cross-shore front resembles a gravity current and is generated by a convergent strain field acting on the large scale density field. The ensemble front is bounded by the shoreline and is alongfront geostropic and cross-front ageostrophic. This contrasts with the cross-front geostrophic and along-front ageostrophic balances of classic deformation frontogenesis, but is consistent with semi-geostrophic coastal circulation.

1. Introduction

The sea surface density field contains rich variability over submesoscale $O(0.1-10\,\mathrm{km})$ length-scales (*e.g.,* McWilliams 2016) that often manifest as density fronts and filaments. Previous studies have shown that submesoscale fronts and filaments in the open ocean (100s km from shore) can affect the transport of biogeochemical tracers and contaminants (*e.g.,* Franks 1992; Nagai et al. 2015; Mahadevan 2016; Lévy et al. 2018). Submesoscale density fronts are ubiquitous on continental shelves in high resolution coastal models (*e.g.,* Romero et al. 2016; Dauhajre et al. 2017, 2019), observed within $10\,\mathrm{km}$ from shore (*e.g.,* Ohlmann et al. 2017; Connolly and Kirincich 2019), and detected in satellite sea surface temperature (SST) images (*e.g.,* Castelao et al. 2006; Kahru et al. 2012). Dye and SST observations reveal frontal variability within 1 km from shore (Hally-Rosendahl et al. 2015; Grimes et al. 2020). Fronts alter Lagrangian transport pathways and water mass structure over the continental shelf (*e.g.,* Banas et al. 2009; Rao et al. 2011). Here, we focus on the dynamics of submesoscale fronts in the shallow coastal ocean (< 10 km from shore and < 30 m water depth). In coastal regions at $O(0.1 - 10\,\mathrm{km})$ length-scales, studies have largely focused on fronts associated with inlet and river plumes (*e.g.,* O'Donnell 2010; Chant 2011; Horner-Devine et al. 2015; Feddersen et al. 2016) and upwelling (*e.g.,* Brink 1987; Austin and Barth 2002; Austin and Lentz 2002). Instead, we focus on coastal fronts in a region of weak winds and no significant freshwater flows, a poorly studied part of the coastal submesoscale frontal parameter space.

A companion paper of this work (Wu et al. 2020, hereinafter W20) investigated the processes transporting shoreline released dye representing wastewater off the San Diego(US)/Tijuana(MX) coast in the San Diego Bight (see Fig. 1) using a high-resolution realistic wave-current coupled model. On the mid- to outer shelf boundary (smoothed 25 m isobath, ≈ 5 km from shore), wind-driven Ekman transport and submesoscale flows both played an important role in offshore dye transport during a three month analysis period. The submesoscale flows were elevated for stronger root-mean-square (rms) surface alongshore density gradients at length-scales $< 15\,\mathrm{km}$, which were enhanced by the large scale (over $\approx 15\,\mathrm{km}$ alongshelf) convergent northward alongshore flow, suggesting cross-shore oriented fronts. In high resolution numerical models, density gradients are preferentially perpendicular to bathymetric contours in depths < 50 m (Romero et al. 2013; Dauhajre et al. 2017), suggesting alongshore oriented fronts and filaments. In general, the kinematics (*i.e.,* occurrence likelihood, orientations, lengths, and density gradient magnitude) of coastal (within 10 km of shore) density fronts in regions with little freshwater input are poorly understood.

Mechanisms for both forced and unforced frontogenesis often have been examined with a frontogenesis tendency equation for the material derivative of the horizontal density gradient magnitude squared (*e.g.,* Hoskins 1982; O'Donnell 2010),

$$\frac{D(|\nabla_H \rho|^2)}{Dt} = F \tag{1}$$

where ∇_H denotes the horizontal gradient, F comprises the enhancing (positive F, frontogenetic) or weakening (negative F, frontolytic) driving terms. Many coastal fronts are forced by freshwater input or wind-driven upwelling (Austin and Lentz 2002; Horner-Devine et al. 2015). In shallow water, forcing by tides and bathymetry can generate differential mixing/advection and induce fronts (*e.g.,* Simpson et al. 1978; Huzzey and Brubaker 1988). In the open ocean, *unforced* mechanisms for generating frontogensis have been proposed including deformation frontogenesis (DF, Hoskins and Bretherton 1972) and turbulent thermal wind balance (TTW, McWilliams et al. 2015).

The DF mechanism involves a large-scale geostrophic, non-divergent strain field whose cross-front convergence enhances the density gradient and accelerates an along-front jet, which via Coriolis forcing induces an ageostrophic cross-front flow v_a (Hoskins and Bretherton 1972; Hoskins et al. 1978). The induced v_a and the associated downwelling and upwelling form an ageostrophic secondary circulation (ASC) tilting the isopycnals towards the horizontal (*e.g.,* Bleck et al. 1988; Spall 1995; Thomas et al. 2008). TTW refers to a balance among vertical mixing, Coriolis and pressure gradient forcing (McWilliams et al. 2015), where the ageostrophic Coriolis forcing is balanced by vertical mixing (Garrett and Loder 1981; Thompson 2000; Gula et al. 2014; Wenegrat and McPhaden 2016). Cross-front varying vertical mixing of momentum (*i.e.,* $\partial_z(A_v \partial_z u)$, where A_v is the vertical eddy viscosity and u is the alongfront velocity) can induce a cross-front ageostrophic convergence $\partial v_\mathrm{a}/\partial y \neq 0$, enhancing the density gradient and forming a TTW ASC (McWilliams 2017). In numerical models in the Gulf of Mexico, the density gradient of TTW generated fronts and filaments can strengthen rapidly on hourly time scales consistent with an asymptotic model assuming weak near-surface stratification (Barkan et al. 2019). The TTW mechanism was invoked to explain the strengthening of coastal density filaments and fronts during winter and spring in a high resolution numerical model (Dauhajre et al. 2017). However, to what extent the DF and TTW mechanisms are generally applicable to generation of density fronts in coastal regions within

10 km from shore is unclear. Stratification and wind forcing in coastal regions vary dramatically. The spatial variability of horizontal density gradient varies seasonally in the California Current System (Kahru et al. 2012; Mauzole et al. 2020) and in the Gulf Stream (Callies et al. 2015). The shoreline limits the onshore extent of fronts, the shore normal velocity vanishes at the shoreline, and shallow coastal depths constrain frontal vertical circulation. The shoreline also constrains shelf circulation to largely a geostrophic (ageostrophic) balance in the cross-shore (alongshore) direction (*e.g.,* Allen 1980; Lentz et al. 1999).

Here, we focus on the kinematics and dynamics of coastal density fronts (within $10\,\mathrm{km}$ from shore and < 30 m depth) using a high resolution numerical model of the San Diego Bight (W20). A field study in this region noted the enhancement of a dye alongshore front driven by the internal tide (Grimes et al. 2020). In this region, winds are relatively weak and fresh water input is small, placing focus on unforced (*e.g.,* DF and TTW) frontogenesis mechanisms. An edge detection method is used to isolate individual density fronts. We address three main questions. What are the kinematic properties (*i.e.,* orientation, length and density gradient) of these coastal fronts? For cross-shore oriented fronts, what does a typical front look like? What are the processes responsible for the frontogenesis and can they be classified in the context of open ocean unforced frontogenesis mechanisms? The model configuration, front detection procedure, and front kinematic parameters are given in Section 2. Front kinematic properties and variability are analyzed in Section 3. An ensemble mean cross-shore oriented front is created to quantify frontal circulation in Section 4. Frontogenesis mechanisms are diagnosed through frontogenesis tendency and a momentum balance analysis in Sections 5 and 6, respectively. Front dynamics in the context of DF and TTW mechanisms are discussed in Section 7. A summary is provided in Section 8.

2. Model configuration and front detection

a. Model setup

Shelf and surfzone circulation is simulated using the Coupled Ocean-Atmosphere-Wave-Sediment-Transport (COAWST) model system (Warner et al. 2010; Kumar et al. 2012). A full description of the model setup is found in W20. Here only the information essential to this work is provided. The model consists of three one-way nested parent runs (from LV1 to LV2 and then LV3) spanning from the California Current System to the south Southern California Bight, and one downscaled high-resolution child run (LV4) resolving the outer to inner shelf and surfzone in the southern San Diego Bight (Fig. 1). LV4 incorporates surface waves by coupling the Regional Ocean Modeling System (ROMS, Shchepetkin and McWilliams 2005) with the Simulating WAves Nearshore model (SWAN, Booij et al. 1999). NOAA/NAM surface fluxes (wind stress, heat and precipitation) are applied. Vertical mixing (eddy viscosity and diffusivity) is derived from a $k - \epsilon$ submodel (*e.g.,* Umlauf and Burchard 2003) with Kantha and Clayson (1994) stability functions. In all simulations, a 3rd order upwind advection scheme is used for momentum. The horizontal eddy viscosity and diffusivity are constant at $0.5\,\mathrm{m^2s^{-1}}$ over all the model runs. For the LV4 grid, this horizontal eddy viscosity and diffusivity have little effect on submesoscale variability (W20).

The LV4 grid ($15 \times 36\,\mathrm{km}^2$) spans from Punta Bandera (PB), Mexico to Point Loma, US, encompassing the Tijuana River Estuary (TJRE) and the San Diego Bay (SDB) (Fig. 1). The shoreline is relatively straight, except for curvature around SDB and a broad $15\,\mathrm{m}$ depth shoal offshore of the TJRE mouth. The horizontal grid resolution transitions from 100 m along the three open boundaries to 8 m approaching the TJRE mouth, resulting in a regional mean resolution $\approx 30\,\mathrm{m}$. The vertical stretched grid has 15 $s-$levels with enhanced resolution near the surface and bottom. The number of vertical levels is limited to prevent thin vertical layers in very shallow (< 1 m) depths. As we are focused on surface density fronts, we provide context of vertical grid resolution. In 30 m depth, the average vertical resolution is $\Delta z = 0.8$ m for $z > -5$ m and for $-10 < z < -5$, the average vertical resolution is $\Delta z = 2$ m. The initial and boundary conditions, nested from the parent LV3 solution, include both barotropic and baroclinic tides. Barotropic tides are prescribed on the outmost LV1 grid, allowing for the generation of baroclinic tides within all model domains (*e.g.,* Kumar et al. 2015; Suanda et al. 2017; Kumar et al. 2019). LV4 receives realistic freshwater discharge from PB, TJRE and the Sweetwater River within SDB. TJRE discharge occurs following intermittent rainfall events. At PB, untreated wastewater outflows are represented with a constant freshwater discharge ($Q_r = 1.53\,\mathrm{m^3s^{-1}}$, see W20 for more details). The simulation is conducted from July to October 2015 using XSEDE resources (Towns et al. 2014), and solutions are saved at 1-hour intervals.

FIG. 1

b. Regional oceanographic conditions

Following W20, model results are analyzed over the summer to fall transition (22 July to 18 October 2015, denoted *analysis period*). The barotropic mixed tides have an amplitude around $1\,\mathrm{m}$ (Fig. 2a). NAM winds are mostly southeastward directed and have a low ($|\mathbf{U_w}| < 5\,\mathrm{m\,s^{-1}}$) to moderate ($5-8\,\mathrm{m\,s^{-1}}$) speed (Fig. 2b). The shelf stratification is represented by the top-to-bottom buoyancy frequency $N^2 = -(g/\rho_0)\Delta\rho/\Delta z$ at a central location denoted SB ($30\,\mathrm{m}$ depth, see Fig. 1 for location), where g is gravity and the background density $\rho_0 = 1025\,\mathrm{kg\,m^{-3}}$. The subtidal (low-pass filtered with a 33 h cutoff) N^2 decreases overall from a relatively strong $5\times10^{-4}\,\mathrm{s^{-2}}$ during summer to $1\times10^{-4}\,\mathrm{s^{-2}}$ during fall (Fig. 2c), typical for summer to fall stratification in this region of Southern California (*e.g.,* Palacios et al. 2004). Within the LV4 grid, the time-mean surface density has a weak north-south gradient reaching a mid-shelf (25 m isobath) magnitude of $6\times10^{-6}\,\mathrm{kg\,m^{-4}}$ with lighter water to the north (W20). This is due to the regional differences in upwelling between the Southern California and Baja CA (*e.g.,* Huyer 1983) which is also seen in the parent LV3 grid (W20). The SDB has negligible freshwater input during this time period (W20), however, the warm water of the SDB serves as a weak buoyancy source, which may slightly augment this already present N/S regional density gradient. The subtidal depth-averaged alongshore flow at SB, V_{SB}, varies between -0.1 to $0.3\,\mathrm{m\,s^{-1}}$ and is mostly positive (northward directed, Fig. 2d). Diurnal (DU, 33^{-1} to $16^{-1}\,\mathrm{cph}$) baroclinic velocities are significant in this region. Following W20, a complex EOF derived cross-shore (cross-isobath) surface diurnal velocity $u_{\mathrm{DU}}^{(1)}(t)$ is estimated on a smoothed 25 m depth contour. The diurnal velocity $u_{\mathrm{DU}}^{(1)}$ has a modulating amplitude around $0.1\,\mathrm{m\,s^{-1}}$ (Fig. 2d), that weakens with the reduced N^2 later in the analysis period. FIG. 2

FIG. 3

c. *Surface density front identification*

FIG. 4

Surface density fronts frequently occur during the analysis period, as shown in the two examples (Fig. 3). In the first example, the $\approx 6\,\mathrm{km}$-long surface density front is steeply angled relative to the cross-shore direction and is mostly onshore of the 25 m isobath (Fig. 3a). This front was compressed in the alongshore direction by the convergent alongshore flow (as described in W20, Fig. 3 therein). In the second example, the surface density front is much more aligned in the cross-shore direction with a length of $\approx 5\,\mathrm{km}$ (Fig. 3b).

Both example density fronts are primarily located within the *front study region* (see white box in Fig. 1), a bounded region ($5.5\times18.5\,\mathrm{km^2}$) that extends from the shoreline to the $\approx 30\,\mathrm{m}$ isobath and spans the surfzone through mid-shelf. The region's southern and northern boundaries are $5\,\mathrm{km}$ away from the grid's southern open boundary and $7\,\mathrm{km}$ from the SDB mouth, respectively. Surface density fronts primarily contained within this study region are the focus of this work.

Modeled surface density fronts are identified by applying the Canny edge detection algorithm (Canny 1986) to the surface density. This algorithm has been successfully applied to front detection in SST satellite images (*e.g.,* Castelao et al. 2006; Jones et al. 2012). The algorithm first interpolates the surface density onto an equally-spaced horizontal grid with $\Delta = 40\,\mathrm{m}$ resolution, coarser than the grid mean resolution ($\approx 30\,\mathrm{m}$) to preserve data quality. Then, density is smoothed using a 2-D Gaussian filter with a $\sqrt{2}\Delta$ standard deviation (std). The horizontal density gradient $\nabla_H \rho$ is computed by convoluting the smoothed density with the spatial derivative of the 2-D Gaussian filter (Canny 1986). The algorithm finds grid points with $|\nabla_H \rho|$ larger than a threshold $|\nabla_H \rho|_\mathrm{c}$ (described below), which are labeled as a *front*. Thereafter, the algorithm tracks the grid points that are connected to the front with a $|\nabla_H \rho|$ larger than a smaller threshold $c|\nabla_H \rho|_\mathrm{c}$ ($c = 0.4$, following Castelao et al. 2006), adding these grid points to the front. This approach results in more contiguous fronts and reduces multiple patchy fronts. The algorithm is applied to each hour of model outputs over the analysis period. Note that, some fronts detected at consecutive time steps are the same front advected to a new location. For simplicity, frontal evolution is not considered here and each identified front at each time step is considered separately.

For our analysis, we focus on fronts that are relatively straight, are longer than 4 km, and are not strongly affected by open boundaries, SDB outflow, or the surfzone. Thus, we apply the following criteria to reject fronts identified by the edge detection algorithm. First, the mean front location (*i.e.,* center of mass of the front, green dot in Figs. 3a,b) must be located within the front study region. Second, the offshore end of the front must be at least 1.5 km from the shoreline, to ensure that surfzone processes are not dominating the front. Third, the front is fit to an ellipse. To ensure relatively straight fronts, we require that the ratio of the ellipse minor to major axes $\gamma < 0.15$. Fourth, we require that the front length is > 4 km. Both example fronts (Fig. 3) pass the criteria as their mean location is within the front study region, their lengths are > 4 km, and their $\gamma = 0.06$ and $\gamma = 0.04$.

Applying the edge detection algorithm and four criteria, the total number of detected fronts N_f over the analysis period (2112 hours) is a function of the threshold $|\nabla_H \rho|_\mathrm{c}$ (Fig. 4). As $|\nabla_H \rho|_\mathrm{c}$ increases from $0.2\times$ to $12.3 \times 10^{-4}\,\mathrm{kg\,m^{-4}}$, the total count decreases from $N_\mathrm{f} = 6742$ to $N_\mathrm{f} = 371$

(Fig. 4), and the mean hourly front count decreases from 3.2 to 0.17. For the following analysis, we choose the $|\nabla_H \rho|_\mathrm{c}$ threshold as the inflection of the curve (triangle in Fig. 4, $|\nabla_H \rho|_\mathrm{c} = 2.9 \times 10^{-4}\,\mathrm{kg\,m^{-4}}$). This choice requires fronts to have a relatively strong density gradient while it allows sufficient fronts ($N_\mathrm{f} = 2948$) for statistical analyses. The lower cutoff $c|\nabla_H \rho|_\mathrm{c} = 1.2 \times 10^{-4}\,\mathrm{kg\,m^{-4}}$ is comparable to the upper-end of the smoothed 25 m isobath root-mean-square (rms) alongshore density gradient $1.5\times 10^{-4}\,\mathrm{kg\,m^{-4}}$ (W20).

For the $N_\mathrm{f} = 2948$ selected fronts, kinematic front parameters are defined. First, a front axis is defined as the least-square fit line to the front (see magenta dashed line in Figs. 3a,b). A front orientation angle θ_f ($\theta_\mathrm{f} \in [-90^\circ, 90^\circ]$) is the angle between the mean shoreline normal direction (5° clockwise from the grid cross-shore orientation, see cyan line in Fig. 3a) and the front axis (see Fig. 3a). For fronts that tilt northward offshore, $\theta_\mathrm{f} < 0^\circ$ (Fig. 3a). The front length L_f is defined as the length of the front projected onto the front axis (Fig. 3b). The along-front mean surface density gradient $|\nabla_H \rho|_\mathrm{f}$ is calculated by averaging the surface $|\nabla_H \rho|$ along the bending front. Note that $|\nabla_H \rho|_\mathrm{f}$ magnitude must be $\geq c|\nabla_H \rho|_\mathrm{c}$. For reference, the first example front (Fig. 3a) has $\theta_\mathrm{f} = -54^\circ$, $L_\mathrm{f} = 5.9$ km, and $|\nabla_H \rho|_\mathrm{f} = 3.0 \times 10^{-4}\,\mathrm{kg\,m^{-4}}$ and the second example front (Fig. 3b) has $\theta_\mathrm{f} = 6^\circ$, $L_\mathrm{f} = 5.5$ km, and $|\nabla_H \rho|_\mathrm{f} = 5.6 \times 10^{-4}\,\mathrm{kg\,m^{-4}}$.

3. Kinematic frontal properties

a. Kinematic front parameter statistics

FIG. 5

Here, a statistical analysis on the kinematic front parameters (θ_f, L_f, $|\nabla_H \rho|_\mathrm{f}$, and front mean location) is performed on the $N_\mathrm{f} = 2948$ selected fronts. The front orientation angle θ_f histogram has a U-shaped distribution (Fig. 5a) with maxima near ±90° (fronts aligned with the shoreline) and a minima near $\theta_\mathrm{f} = 0^\circ$ (fronts shore-normal oriented). The prevalence of alongshore oriented fronts is generally consistent with modeled inner- to mid-shelf density gradients preferentially aligned across isobath (Romero et al. 2013; Dauhajre et al. 2017). Based on the θ_f distribution, fronts are categorized into alongshore oriented, cross-shore oriented, and inclined fronts. Alongshore fronts are defined as having a near-shoreline (within 20°) orientation, that is $\theta_\mathrm{f} \in [-90^\circ, -70^\circ]$ or $\theta_\mathrm{f} \in [70^\circ, 90^\circ]$ (dark gray shading in Fig. 5a). Cross-shore fronts are defined as having an orientation $\theta_\mathrm{f} \in [-50^\circ, 50^\circ]$ (light gray shading in Fig. 5a, an example in Fig. 3b). Separating the alongshore and cross-shore fronts are inclined fronts, defined as having an orientation $\theta_{\mathrm{f}} \in [-70^\circ, -50^\circ]$ or $\theta_{\mathrm{f}} \in [50^\circ, 70^\circ]$ (see example in Fig. 3a). Overall, the alongshore oriented, inclined, and cross-shore oriented fronts account for 55%, 27% and 18% of the total fronts, respectively. Thus, the cross-shore fronts are about 1/3 as numerous as alongshore fronts. The cross-shore fronts have the widest angular range as the cross-shore shear of the alongshore flow can tilt cross-shore fronts. Cross-shore fronts tilting northward offshore ($\theta_{\mathrm{f}} < 0^\circ$) are more likely than those tiling southward offshore ($\theta_{\mathrm{f}} > 0^\circ$, Fig. 5a), as the alongshore flow is mostly northward directed (see V_{SB} in Fig. 2d).

For all fronts, the front length L_{f} histogram is quasi-exponential with $L_{\mathrm{f}} = 4$ km most likely and the $L_{\mathrm{f}} \geq 16$ km likelihood reduced by factor of 50 (Fig. 5b). The L_{f} histogram for alongshore and cross-shore fronts separately is also quasi-exponential. Alongshore fronts are generally longer than cross-shore fronts. Alongshore fronts have mean (± std) $L_{\mathrm{f}} = 7.8(\pm 3.4)$ km, while cross-shore fronts have mean (± std) $L_{\mathrm{f}} = 5.8(\pm 1.8)$ km. Longer cross-shore fronts ($L_{\mathrm{f}} > 8$ km) are more likely for more negative $\theta_{\mathrm{f}} \approx -50^\circ$. The grid offshore boundary is ≈ 10 km from the shoreline and the grid alongshore dimension is 36 km, possibly limiting cross-shore and alongshore front L_{f}.

For all fronts, the along-front averaged density gradient $|\nabla_H \rho|_{\mathrm{f}}$ histogram is skewed with maxima at $|\nabla_H \rho|_{\mathrm{c}}$ and an exponential decrease for larger $|\nabla_H \rho|_{\mathrm{f}}$ (Fig. 5c). The $|\nabla_H \rho|_{\mathrm{f}}$ can vary by a factor of 10, from $2\times$ to $20 \times 10^{-4}\,\mathrm{kg\,m^{-4}}$. Although the alongshore fronts are more numerous, both alongshore and cross-shore fronts have similar mean $|\nabla_H \rho|_{\mathrm{f}}$ with values of $4.2 \times 10^{-4}\,\mathrm{kg\,m^{-4}}$ and $3.9 \times 10^{-4}\,\mathrm{kg\,m^{-4}}$, respectively. For both cross-shore and alongshore fronts, no relationship between $|\nabla_H \rho|_{\mathrm{f}}$ and θ_{f} is evident (not shown). Two-thirds of the alongshore fronts have a positive mean cross-front density gradient (denser water onshore). For the cross-shore fronts, 90% have negative mean density gradient (lighter water to the north). The $|\nabla_H \rho|_{\mathrm{f}}$ of cross-shore fronts are $\approx 2\times$ larger than the rms alongshore density gradient along a smoothed 25 m depth contour (W20).

FIG. 6

Next, the spatial distribution of the cross- and alongshore fronts is examined for preferred frontal position within the front study region. For example, the intermittent TJRE discharge and the TJRE shoal may promote local frontogenesis. The $N_{\mathrm{f}} = 528$ cross-shore fronts are present throughout the *frontal study region*, mostly tilting northward offshore (Fig. 6a1). The range of L_{f} and $\nabla_H \rho$ for the cross-shore fronts is also evident. The cross-shore front mean location (center of mass) has $\approx 2/3$ of fronts located northward of the TJRE mouth, and $\approx 1/3$ located south of the TJRE mouth (Fig. 6a2). The alongshore fronts also are present throughout the *frontal study region* (Fig. 6b1). Alongshore front mean cross-shore location is twice as likely to occur at the midpoint of the *frontal study region* rather than its offshore end (Fig. 6b2). Alongshore front mean location is somewhat more likely found south of the TJRE mouth, relative to the north.

b. Cross-shore and alongshore front occurrence frequency

FIG. 7

FIG. 8

The differences in front kinematic parameters (θ_{f}, L_{f}, center of mass, Figs. 5, 6) suggest that different processes are responsible for generating the cross-shore and alongshore fronts. Here, we examine the factors affecting the temporal variability of frontal occurrences and the mean $|\nabla_H \rho|_{\mathrm{f}}$ for both cross-shore and alongshore fronts. The hourly front count $n_{\mathrm{f}}(t)$ is defined as the number of identified fronts for a particular hour. For cross-shore fronts, the hourly front count n_{f} varies between 0 and 5, with a time mean (± std) of $0.25(\pm 0.60)$ (Fig. 7b). Cross-shore front hourly n_{f} are elevated during four time periods (*i.e.,* 02-09 Aug, 29-30 Aug, 08-16 Sep and 12-16 Oct), coincident with the periods of positive (northward) V_{SB} (Fig. 7a). The hourly n_{f} of the alongshore fronts ranges between 0 and 10, with a time mean (± std) of $0.75(\pm 1.2)$ (Fig. 7c). The alongshore front n_{f} is not related to V_{SB}. Alongshore fronts are detected for 84 out of 88 days of the analysis period (*i.e.,* 95% of the period), and the n_{f} have consistent diurnal variability.

To further investigate the relationship between frontal temporal variability and flow conditions, the cross-shore and alongshore hourly n_{f} are bin-averaged using V_{SB} and the surface diurnal velocity $u_{\mathrm{DU}}^{(1)}$ (Section 2b) in Fig. 8. For cross-shore fronts, the bin-mean hourly $n_{\mathrm{f}} < 0.1$ for negative (southward) V_{SB}, and increases with positive (northward) V_{SB} to $n_{\mathrm{f}} \approx 0.7$ for $V_{\mathrm{SB}} \approx 0.25\ \mathrm{m\,s^{-1}}$ (Fig. 8a). This is consistent with the elevated rms alongshore density gradient along the smoothed 25 m isobath for stronger northward V_{SB} (W20). The bin-mean front density gradient $|\nabla_H \rho|_{\mathrm{f}}$ is slightly elevated for $V_{\mathrm{SB}} > 0.1\ \mathrm{m\,s^{-1}}$ compared with that when $V_{\mathrm{SB}} < 0.1\ \mathrm{m\,s^{-1}}$. The binned mean cross-shore front n_{f} has no relationship to the SDB outflow velocity at zero to 6 h time-lag (not shown). This indicates that SDB-sourced buoyancy is not generating the cross-shore fronts. The binned mean cross-shore front n_{f} also has no relationship to the alongshore (grid aligned) subtidal wind stress nor the surface baroclinic diurnal velocity $u_{\mathrm{DU}}^{(1)}$ (not shown). Overall, this indicates that northward alongshore flow on 2–7 day time-scales affects the generation of cross-shore fronts.

For the alongshore fronts, the binned-mean hourly n_{f} is small (≤ 0.5) for $u_{\mathrm{DU}}^{(1)} < 0\ \mathrm{m\,s^{-1}}$ (offshore directed) and increases for positive $u_{\mathrm{DU}}^{(1)}$ (onshore directed) to $n_{\mathrm{f}} > 1$ for $u_{\mathrm{DU}}^{(1)} > 0.05\ \mathrm{m\,s^{-1}}$ (Fig. 8b). The bin-mean $|\nabla_H \rho|_{\mathrm{f}}$ is also generally elevated for larger positive $u_{\mathrm{DU}}^{(1)}$ (Fig. 8b). The alongshore front binned-mean n_{f} was not related to V_{SB} but weakly related to the alongshore (grid aligned) subtidal wind stress with slightly elevated n_{f} (and $|\nabla_H \rho|_{\mathrm{f}}$) for the strongest downwelling winds versus strongest upwelling winds (not shown). Note, however that winds were generally weak during the analysis period (Fig. 2b). This suggests that the alongshore fronts are forced by the onshore surface flow of diurnal baroclinic tides, which are significant in the region (W20) even though they are subcritical at this latitude.

4. Ensemble mean cross-shore front

Individual cross-shore fronts have variable orientation θ_{f}, frontal length L_{f}, and frontal density gradient $|\nabla_H \rho|_{\mathrm{f}}$. These fronts can be slightly curved and the front may deviate from the front axis. To better understand the characteristics and dynamics of the cross-shore fronts, an ensemble mean cross-shore front is created in the following analysis. Analysis of alongshore fronts will be further investigated elsewhere.

FIG. 9

a. Cross-shore front extraction, front decomposition, and ensemble average

To diagnose ensemble cross-shore front dynamics, individual cross-shore fronts are first extracted, variables are decomposed into cross-front mean and perturbation components, and an ensemble mean cross-shore front is then generated on a subset of the cross-shore fronts. Each cross-shore front is extracted using a rectangular control volume, centered along the best-fit front axis, with horizontal dimensions of 4 km cross-front and 8 km along-front where the onshore end of the control volume intersects the shoreline. Control volumes for the two example fronts are shown in Figs. 3a,b. Within the control volume, an along-front coordinate ($\tilde{x}$, positive onshore) is defined with $\tilde{x} = 0$ at the shoreline intersection (Fig. 3b). The cross-front coordinate ($\tilde{y}$, positive northward) is defined with $\tilde{y} = 0$ at the front axis (see Fig. 3b). The origin $(\tilde{x}, \tilde{y}) = (0, 0)$ m is on the shoreline (Fig. 3b). The flow is then decomposed into along-front (u) and cross-front (v) components.

The extracted cross-shore fronts ($N_{\mathrm{f}} = 528$, Fig. 6a) have a wide range of θ_{f}. Some cross-shore fronts may interact with adjacent fronts detected at the same time. Most but not all cross-shore fronts have a negative cross-front density gradient $\partial\rho/\partial\tilde{y}$ (Section 3a). Ensemble analysis focuses on cross-shore fronts that do not interact with other fronts, have a smaller θ_{f} range, span across the inner to mid-shelf, and have a consistent cross-front density gradient sign. Thus we generate a subset of cross-shore fronts, termed test fronts that satisfy four additional criteria: (1) For a particular cross-shore front, all other fronts detected at the same time step must be separated by > 4 km (the control volume width). This criterion reduces the total cross-shore front count from 528 to 431. (2) Cross-shore fronts should be roughly shore-normal requiring the front orientation angle $\theta_\mathrm{f} \in [-25°, 25°]$, removing an additional 299 fronts. A wider θ_f range (*e.g.,* $\pm 45°$) obtains consistent results for the subsequent analyses (not shown here). (3) The front must reach the $25\,\mathrm{m}$ isobath (see Fig. 3b) and must span $-6 < \tilde{x} < -4$ km within the control volume (black contour in Fig. 3c), ensuring the front spans across the inner to mid-shelf, and allowing an along-front average over this region. This criteria excludes an additional 42 fronts. (4) To ensure consistent ensemble front dynamics, the cross-front density gradient $\partial\rho/\partial\tilde{y}$ must be negative, excluding four remaining fronts with positive $\partial\rho/\partial\tilde{y}$. These four fronts are associated with the northern side of cross-shore oriented warm filaments that occur infrequently.

These criteria together result in a subset of 86 cross-shore test fronts (Fig. 9). The example cross-shore front in Fig. 3b is also a test front. The test fronts mostly tilt gently northward offshore, and their θ_f (red bar in Fig. 5a) are mostly negative with mean ($\pm$ std) of $-10.5°(\pm 12.3°)$. The test fronts are concentrated north of the TJRE mouth (Fig. 9). The test fronts have a mean $L_\mathrm{f} = 5.9\,\mathrm{km}$, similar to mean $L_\mathrm{f} = 5.8$ km for all cross-shore fronts. In addition, the test fronts have a mean $|\nabla_H \rho|_\mathrm{f} = 3.5 \times 10^{-4}\,\mathrm{kg\,m^{-4}}$, also similar to the mean of $3.9 \times 10^{-4}\,\mathrm{kg\,m^{-4}}$ for all cross-shore fronts (Section 3a). This suggests that the 86 test fronts are representative of the set of all cross-shore fronts. Consistent with the entire set of cross-shore fronts, test fronts occur (red line in Fig. 7b) only for $V_\mathrm{SB} \geq 0.08\,\mathrm{m\,s^{-1}}$ and also have stronger density gradient for $V_\mathrm{SB} > 0.16\,\mathrm{m\,s^{-1}}$ (not shown). Among the test fronts, 56 fronts are from 17 fronts that are extracted at multiple (2–6) times as the front is advected. The other 30 fronts are unique and extracted only once. Overall, 47 unique fronts are included.

For each of the 86 test fronts, cross-front mean and perturbation components for variable ψ_i (at each $z-$level if depth-dependent) are defined as

$$\psi_i(\tilde{x},\tilde{y}) = \overline{\psi_i}^{\tilde{y}}(\tilde{x}) + \psi_i'(\tilde{x},\tilde{y}) \tag{2}$$

where i denotes front number and $\overline{()}^{\tilde{y}}$ denotes a cross-front average over the $4\,\mathrm{km}$ wide control volume, and the prime represents the perturbation. This decomposition is applied to the along-front, cross-front and vertical velocity components (u, v, w), relative vertical vorticity $\zeta = \partial v/\partial\tilde{x} - \partial u/\partial\tilde{y}$, divergence $\delta = \partial u/\partial\tilde{x} + \partial v/\partial\tilde{y}$, temperature T, salinity S, density ρ and sea surface elevation η. This decomposition for the surface density ρ' and perturbation (u', v') vectors is shown for the cross-shore front example (Fig. 3c). The perturbation density ρ' has a strong cross-front gradient and weaker along-front gradient, particularly in the region of the identified front ($-7 < \tilde{x} < -1.5$ km, Fig. 3c). The front is also associated with a velocity convergence at the front axis $\tilde{y} = 0$ m.

The individual test fronts can be complex, have variable orientations, and span a range of depths. To analyze a mean front, we ensemble average over all test fronts. The front ensemble mean, denoted with $\langle\ \rangle$, applied to the cross-front averaged and perturbation components, is estimated using all $N_c = 86$ test fronts, for example, for T',

$$\langle T'\rangle(\tilde{x}, \tilde{y}, z) = \frac{1}{N_c}\sum_{i=1}^{N_c} T'_i. \tag{3}$$

The ensemble average (Eq. 3) is estimated at a particular $(\tilde{x}, \tilde{y}, z)$ location only if $(\tilde{x}, \tilde{y}, z)$ is wet for all the 86 test fronts. This limits in particular the depth range over which the ensemble average can be estimated using all 86 test fronts. The ensemble average results in a smooth ensemble front as individual fronts are not straight. Note, an ensemble average generally implies averaging individual realizations drawn from the same random variable. However, these individual test fronts span 3 months, with varying winds, flows, and stratification (Fig. 2), and, as noted, are complex (Fig. 3c). Thus, these test fronts are unlikely to be members of the same random variable.

In some analyses that examine a vertical cross-front section, to further remove noise, an along-front average between $(-6 < \tilde{x} < -4)$ km, denoted with $\overline{()}^{\tilde{x}}$, of the ensemble mean variables is performed, for example,

$$\overline{\langle T'\rangle}^{\tilde{x}}(\tilde{y}, z) = \frac{1}{2\ \text{km}}\int_{\tilde{x}=-6\ \text{km}}^{\tilde{x}=-4\ \text{km}} \langle T'\rangle\, d\tilde{x}, \tag{4}$$

FIG. 10

Recall that all test fronts are required to have a front within $-6 < \tilde{x} < -4$ km range (*e.g.,* Fig. 3c).

b. Ensemble and cross-front averaged test front

FIG. 11

FIG. 12

The ensemble and cross-front mean variables represent the ensemble background shelf conditions associated with the test fronts (Fig. 10). The ensemble and cross-front mean sea surface elevation $\langle\overline{\eta}^{\tilde{y}}\rangle$ has a maximum near $\tilde{x} \approx -1.5$ km and tilts downward farther offshore (along-front) while steepening slightly (Fig. 10a). The ensemble and cross-front mean density $\langle\overline{\rho}^{\tilde{y}}\rangle$ varies from near-surface $1023.0\ \mathrm{kg\,m^{-3}}$ to $1023.5\ \mathrm{kg\,m^{-3}}$ at $z = 10$ m (Fig. 10b) with stratification stronger near surface ($N^2 \approx 6 \times 10^{-4}\,\mathrm{s^{-2}}$ at $z = -2$ m) and weakening to $N^2 \approx 3 \times 10^{-4}\,\mathrm{s^{-2}}$ at $z = -10$ m. These values are consistent with the time mean top-to-bottom $N^2 = 3 \times 10^{-4}\,\mathrm{s^{-2}}$ at SB in 30 m depth (Fig. 2c). The ensemble and cross-front mean currents $\langle \overline{u}^{\tilde{y}} \rangle$ and $\langle \overline{v}^{\tilde{y}} \rangle$ represent the ensemble background flow advecting the front (Figs. 10c,d). The along-front component $\langle \overline{u}^{\tilde{y}} \rangle$ is offshore (along-front) directed, weaker at depth, and strengthens offshore from $\approx 0.02\ \mathrm{m\,s^{-1}}$ at $\tilde{x} = -2$ km to $\approx -0.12\ \mathrm{m\,s^{-1}}$ at $\tilde{x} = -8$ km (Fig. 10c). The along-front averaged (from $-8 < \tilde{x} < -2$ km) along-front divergence in the upper 10 m is $\partial \langle \overline{u}^{\tilde{y}} \rangle / \partial \tilde{x} = 1.8 \times 10^{-5}\ \mathrm{s^{-1}}$ ($0.23f$). The cross-front component $\langle \overline{v}^{\tilde{y}} \rangle$ is all positive (northward directed), maximum at $z \approx -5$ m, and strengthens offshore from $\langle \overline{v}^{\tilde{y}} \rangle \approx 0.06\ \mathrm{m\,s^{-1}}$ at $\tilde{x} = -2$ km to $\langle \overline{v}^{\tilde{y}} \rangle \approx 0.14\ \mathrm{m\,s^{-1}}$ at $\tilde{x} = -8$ km (Fig. 10d). The depth-averaged $\langle \overline{v}^{\tilde{y}} \rangle$ is largely in balance with ensemble and cross-front averaged barotropic pressure gradient (PG) induced by $\langle \overline{\eta}^{\tilde{y}} \rangle$ (Fig. 10a), consistent with classic cross-shelf depth-averaged momentum balances (*e.g.,* Allen 1980).

The ensemble mean of the cross-front perturbation variables reveal a clear front that has dense ($-2 < \tilde{y} < 0\,\mathrm{km}$) and light ($0 < \tilde{y} < 2\,\mathrm{km}$) sides (Fig. 11a), strong cross-front gradients, and much weaker alongfront gradients. The perturbation $\langle \eta' \rangle$ varies largely ± 0.001 m over the control volume (Fig. 11a). The strong cross-front gradient $\partial \langle \eta' \rangle / \partial \tilde{y} \approx 10^{-6}$ is consistent with the offshore $\langle \overline{u}^{\tilde{y}} \rangle \approx 0.12\,\mathrm{m\,s^{-1}}$ (Fig. 10c) being largely in geostrophic balance. Weaker along-front $\langle \eta' \rangle$ gradient $\partial \langle \eta' \rangle / \partial \tilde{x}$ has opposite signs on the dense and light side of the front. The near-surface ($z = -1\,\mathrm{m}$) perturbation temperature $\langle T' \rangle$ varies strongly in the cross-front direction and much more weakly in the alongfront ($\tilde{x}$) direction (Fig. 11b). In the main region of the front ($-6 < \tilde{x} < -4$ km), $\langle T' \rangle$ varies cross-front by $0.3\,^{\circ}\mathrm{C}$ within ± 0.5 km of the front axis. The cross-front perturbation density $\langle \rho' \rangle$ is dominated by temperature (salinity not shown) and varies by $\approx 0.1\ \mathrm{kg\,m^{-3}}$ across ± 0.5 km of the front axis with gradient enhanced at the front axis (Fig. 11c). The perturbation along-front velocity $\langle u' \rangle$ is generally small (0–0.02 $\mathrm{m\,s^{-1}}$), much smaller than $\langle \overline{u}^{\tilde{y}} \rangle$, with decreasing magnitude towards the shoreline and switches sign on either side of the ensemble front (Fig. 11d). On both sides of the front, the spatial average of $\partial \langle u' \rangle / \partial \tilde{x} \approx \pm 0.03f$, much weaker than the spatial mean $\partial \langle \overline{u}^{\tilde{y}} \rangle / \partial \tilde{x} \approx 0.23f$. The perturbation cross-front velocity $\langle v' \rangle$ varies from $0.04\,\mathrm{m\,s^{-1}}$ to $-0.04\,\mathrm{m\,s^{-1}}$ from the dense to light side of the front, (Fig. 11e), around one third the magnitude of $\langle \overline{v}^{\tilde{y}} \rangle$ (Fig. 10d). The maximum cross-front convergence $\partial \langle v' \rangle / \partial \tilde{y} \approx -1.2f$ occurs parallel to the front axis, but shifted slightly to the dense side $\tilde{y} \approx -0.3$ km, and is partially balanced by the divergence of the along-front flow $\partial\langle\overline{u}^{\tilde{y}}\rangle/\partial\tilde{x}$. For $\tilde{x} \leq -4\,\mathrm{km}$, negative (downwelling) vertical velocity $\langle w'\rangle \approx -1 \times 10^{-4}\,\mathrm{m\,s^{-1}}$ occurs just on the dense side of the front axis ($-0.5 < \tilde{y} < 0$ km, Fig. 11f). Farther from the front axis, $\langle w'\rangle$ is mostly weakly positive.

To analyze the cross-front and vertical structure of the ensemble front, we additionally along-front average ensemble-mean perturbation variation within $-6 < \tilde{x} < -4$ km (*e.g.,* $\overline{\langle T'\rangle}^{\tilde{x}}$ in Eq. (4), Fig. 12b). Only the top $10\,\mathrm{m}$ is presented and analyzed as the test fronts minimum water depth at $\tilde{x} = -4$ km is $13\,\mathrm{m}$. Many aspects of the upper-water column ($z > -3$ m) along-front averaged variables (Fig. 12) mirror those in Fig. 11. The ensemble front is generally enhanced near-surface (Fig. 12). The cross-front structure of $\overline{\langle S'\rangle}^{\tilde{x}}$ has subsurface extrema (Fig. 12a). Cross-front salinity gradients contribute minimally to cross-front density gradients but act constructively with temperature. The cross-front temperature $\overline{\langle T'\rangle}^{\tilde{x}}$ variability is reduced by 1/3 between the upper ($z > -5$ m) and lower ($z < -5$ m) water column. The cross-front location ($\tilde{y}$) of maximum $\partial\overline{\langle T'\rangle}^{\tilde{x}}/\partial\tilde{y}$ is near the front axis at surface and shifts to $\tilde{y} \approx -0.5$ km at $z = -5$ m (Fig. 12b). The perturbation density $\overline{\langle\rho'\rangle}^{\tilde{x}}$ (Fig. 12c) is consistent with $\overline{\langle T'\rangle}^{\tilde{x}}$. The density gradient has a surface maximum at the front axis of $\partial\overline{\langle\rho'\rangle}^{\tilde{x}}/\partial\tilde{y} = -1.9\times10^{-4}\,\mathrm{kg\,m^{-4}}$, which decreases with depth and shifts to $\tilde{y} \approx -0.5$ km, similar to temperature. Within the top $5\,\mathrm{m}$, the perturbation along-front velocity $\overline{\langle u'\rangle}^{\tilde{x}}$ switches sign from dense ($\approx 0.01\,\mathrm{m\,s^{-1}}$ at $\tilde{y} < -0.5$ km) to light ($\approx -0.01\,\mathrm{m\,s^{-1}}$) sides of the front (Fig. 12d). For $z < -5$ m, the sign of $\overline{\langle u'\rangle}^{\tilde{x}}$ reverses relative to near surface with diagonally sloped $\overline{\langle u'\rangle}^{\tilde{x}} = 0\,\mathrm{m\,s^{-1}}$ contours. The cross-front velocity $\overline{\langle v'\rangle}^{\tilde{x}}$ variability is also reduced by $\approx 1/3$ between the upper ($z > -5$ m) and lower ($z < -5$ m) water column (Fig. 12e). The ensemble mean perturbation vertical velocity $\overline{\langle w'\rangle}^{\tilde{x}}$ is near zero ($O(10^{-6})\,\mathrm{m\,s^{-1}}$) at the surface, is generally downwelling on the dense side ($\tilde{y} < 0$ km) and upwelling ($\approx 0.4 \times 10^{-4}\,\mathrm{m\,s^{-1}}$) on the light side ($\tilde{y} > 0$ km) of the front (Fig. 12f), significantly larger than root-mean-square $\langle\overline{w}^{\tilde{y}}\rangle = 0.1 \times 10^{-4}\,\mathrm{m\,s^{-1}}$ in the region $-6 < \tilde{x} < -4$ km.

The ensemble mean perturbation vertical vorticity $\overline{\langle\zeta'\rangle}^{\tilde{x}}$ is generally small ($\pm0.2f$), largely positive (negative) on the dense (light) side (Fig. 12g). This $\overline{\langle\zeta'\rangle}^{\tilde{x}}$ is due to the weak $\overline{\langle u'\rangle}^{\tilde{x}}$ (Fig. 12d) and the sign change of $\overline{\langle\zeta'\rangle}^{\tilde{x}}$ is largely determined by $-\partial\overline{\langle u'\rangle}^{\tilde{x}}/\partial\tilde{y}$. In contrast, the ensemble mean perturbation divergence $\overline{\langle\delta'\rangle}^{\tilde{x}}$ has extrema (maximum convergence) near the front axis (Fig. 12h). The surface maximum convergence is $\overline{\langle\delta'\rangle}^{\tilde{x}} \approx -0.8f$, slightly shifted to the dense side ($\tilde{y} = -0.3$ km), as expected from the $\overline{\langle v'\rangle}^{\tilde{x}}$ result (Fig. 12e). The maximum convergence weakens downward and reaches $-0.2f$ at $z = -5\,\mathrm{m}$. Note that, at each z–level $\overline{\langle\delta'\rangle}^{\tilde{x}}$ has a $\tilde{y}$–mean of 0 by definition, thus

$\overline{\langle \delta' \rangle}^{\tilde{x}}$ can have positive values while $\overline{\langle v' \rangle}^{\tilde{x}}$ is consistently convergent over the $10\,\mathrm{m}$ water column (Fig. 12e).

The ensemble averaging of the 86 test fronts with variable lengths, density gradients, and deviation from a straight line results in some smoothing of the resulting ensemble front. We evaluate the smoothing by first examining the coincident parameters of the example front in Figs. 3b,c. The example front density is also temperature dominated and has maximum density gradient $\overline{\partial \rho'/\partial y}^{\tilde{x}} = -3.9 \times 10^{-4}\ \mathrm{kg\,m^{-4}}$, a factor $2\times$ larger than the ensemble front maximum $\overline{\partial \langle \rho' \rangle/\partial y}^{\tilde{x}} = -1.9 \times 10^{-4}\ \mathrm{kg\,m^{-4}}$, as expected because the example front has a relatively strong density gradient (Fig. 5c). The example front cross-front variation in $\overline{u'}^{\tilde{x}}$ and $\overline{v'}^{\tilde{x}}$ are similar to the ensemble front but also a factor $2\times$ stronger. Using the ensemble mean definition (3), we define an ensemble standard deviation as $\mathrm{std}(T') = (\langle (T' - \langle T' \rangle)^2 \rangle)^{1/2}$. The ensemble standard deviation (*e.g.,* $\overline{\mathrm{std}(T')}^{\tilde{x}}$) of perturbation variables S', T', u', and v' are smaller than but of the same order of the ensemble mean with little spatial structure, consistent with the quasi-exponential distribution of the cross-shore oriented front parameters (Fig. 5c). The cross-front ensemble standard deviation density gradient $\overline{\mathrm{std}(\partial \rho'/\partial \tilde{y})}^{\tilde{x}}$ and divergence $\overline{\mathrm{std}(\delta')}^{\tilde{x}}/f$ are elevated within ± 0.5 km of the front axis at magnitudes up to $1.5\times$ the ensemble mean and are weak elsewhere. This is also consistent with the quasi-exponential distribution of density gradient, suggesting that the ensemble mean front is not overly spatially smoothed. FIG. 13

5. Ensemble front frontogenesis tendency

The ensemble mean front exhibits a cross-front density gradient that extends nearly linearly 6–8 km offshore (Fig. 11). Frontogensis can occur through a variety of mechanisms including convergent cross-front flow (*e.g.,* Hoskins and Bretherton 1972), horizontal shear (*e.g.,* Dinniman and Rienecker 1999), and vertical mixing (*e.g.,* Dewey and Moum 1990). Although the ensemble average does not resolve the front evolution history, we examine the local strengthening or weakening of the ensemble front and the responsible processes via a frontogenesis tendency equation analogous to Eq. (1). As $\tilde{y}$ is in the cross-front direction, we only consider the tendency of $(\partial \rho'/\partial \tilde{y})^2$ as

$$\frac{D}{Dt}\left[\left(\frac{\partial \rho'}{\partial \tilde{y}}\right)^2\right] = F_u + F_v + F_w + F_{\mathrm{vmix}} \tag{5}$$

with

$$F_u = -\frac{\partial u'}{\partial \tilde{y}}\frac{\partial \rho}{\partial \tilde{x}}\frac{\partial \rho'}{\partial \tilde{y}} \tag{6a}$$

$$F_v = -\frac{\partial v'}{\partial \tilde{y}}\left(\frac{\partial \rho'}{\partial \tilde{y}}\right)^2 \tag{6b}$$

$$F_w = -\frac{\partial w'}{\partial \tilde{y}}\frac{\partial \rho}{\partial z}\frac{\partial \rho'}{\partial \tilde{y}} \tag{6c}$$

$$F_{\mathrm{vmix}} = \frac{\partial}{\partial \tilde{y}}\left[\frac{\partial}{\partial z}\left(K_\nu \frac{\partial \rho}{\partial z}\right)\right]\frac{\partial \rho'}{\partial \tilde{y}}, \tag{6d}$$

where K_ν is the modeled temporally and spatially varying eddy diffusivity derived from the $k-\epsilon$ scheme (*e.g.,* Umlauf and Burchard 2003). Frontogenesis induced by the cross-front (horizontal) shear is denoted by F_u, and is zero for along-front uniform density. The effect of convergent v' on frontogenesis is given by F_v. Vertical straining deformation is represented by F_w, and F_{vmix} represents the effects of cross-front varying vertical mixing. The ensemble mean of each term is calculated for the 86 test fronts within the control volume and an along-front average (within $-6 < \tilde{x} < -4\,\mathrm{km}$) is then obtained (Fig. 13). Note, the ensemble mean frontogenesis terms are representative of the terms from the individual test fronts.

The cross-front shear induced $\overline{\langle F_u \rangle}^{\tilde{x}}$ is relatively small (Fig. 13a). Within the upper $10\,\mathrm{m}$ and $-2 < \tilde{y} < 2\,\mathrm{km}$, $\overline{\langle F_u \rangle}^{\tilde{x}}$ has a spatial rms $8-30\times$ smaller than the rms of the other three terms. This negligible $\overline{\langle F_u \rangle}^{\tilde{x}}$ is due to the weak along-front density variation $\partial\rho/\partial\tilde{x}$ (Fig. 11c). The cross-front straining deformation $\overline{\langle F_v \rangle}^{\tilde{x}}$ is large and positive near the front axis ($-1 < \tilde{y} < 0.5\,\mathrm{km}$) where $\partial v'/\partial\tilde{y}$ and $\partial\rho/\partial\tilde{y}$ are elevated, and is much weaker farther from the front axis (Fig. 13b). The vertical straining deformation term $\overline{\langle F_w \rangle}^{\tilde{x}}$ (Fig. 13c) is also large and mostly negative near the front axis ($-1 < \tilde{y} < 0.5\,\mathrm{km}$), and weak farther from the front axis. As $\partial\overline{\langle \rho' \rangle}^{\tilde{x}}/\partial\tilde{y} < 0$ (Fig. 12c), the sign of $\overline{\langle F_w \rangle}^{\tilde{x}}$ is due to the the mostly positive $\partial\overline{\langle w' \rangle}^{\tilde{x}}/\partial\tilde{y}$ (Fig. 12f) tilting the isopycnals towards the horizontal. The primarily negative $\overline{\langle F_w \rangle}^{\tilde{x}}$ largely counteracts the cross-front deformation term $\overline{\langle F_v \rangle}^{\tilde{x}}$. The vertical mixing induced $\overline{\langle F_{\mathrm{vmix}} \rangle}^{\tilde{x}}$ (Figs. 13d) is relatively small, mostly positive, and is not concentrated near the front axis. Within $-1 < \tilde{y} < 0.5\,\mathrm{km}$, the spatial rms of $\overline{\langle F_{\mathrm{vmix}} \rangle}^{\tilde{x}}$ is one quarter that of $\overline{\langle F_v \rangle}^{\tilde{x}}$ and $\overline{\langle F_w \rangle}^{\tilde{x}}$. The small $\overline{\langle F_{\mathrm{vmix}} \rangle}^{\tilde{x}}$ implies that density vertical mixing is unimportant to frontogenesis. The total frontogenesis tendency (Fig. 13e), primarily due to $\overline{\langle F_v \rangle}^{\tilde{x}} + \overline{\langle F_w \rangle}^{\tilde{x}}$, is mostly positive implying ensemble mean front strengthening concentrated in a narrow region ($-1 < \tilde{y} < 0.5\,\mathrm{km}$) near the front axis. Near the front axis ($-1 < \tilde{y} < 0.5\,\mathrm{km}$), the horizontally convergent flow (significant $\partial\overline{\langle w' \rangle}^{\tilde{x}}/\partial z$, Fig. 12f) and the large $\overline{\langle F_w \rangle}^{\tilde{x}}$, indicate the importance of ageostrophic processes at the ensemble mean front. Note, the ensemble frontogenesis tendency terms only highlight the material derivative of the ensemble cross-front density gradient comprised of the 86 test fronts, and does not reveal which terms were important at times earlier or later.

6. Ensemble front momentum balance

For the perturbation velocity, no along-front jet develops at the front axis (Fig. 12d), different from both the DF (Hoskins and Bretherton 1972) and TTW (McWilliams 2017) mechanisms, where an along-front jet is in approximate thermal wind balance. The frontogenesis tendency analysis (Fig. 13) indicates the involvement of ageostrophic processes. In the DF and TTW mechanisms, an ageostrophic secondary cross-front flow v_{a} is induced and the ageostrophic Coriolis forcing fv_{a} is balanced by the along-front material acceleration in the DF mechanism (Hoskins et al. 1978), and the vertical mixing in the TTW mechanism (McWilliams et al. 2015). Here the along-/cross-front momentum balances are examined and compared with these mechanisms.

Within the control volume, individual momentum terms in the $(\tilde{x}, \tilde{y})$ directions are decomposed into $\tilde{y}$ mean and perturbation components. The cross-front perturbation momentum balance equations in the $(\tilde{x}, \tilde{y})$ directions are

$$\underbrace{\frac{\partial u'}{\partial t} + \overline{v}^{\tilde{y}}\left(\frac{\partial u'}{\partial \tilde{y}} - \overline{\frac{\partial u'}{\partial \tilde{y}}}^{\tilde{y}}\right)}_{\mathrm{LA'}_{\tilde{x}}} + \underbrace{\left(u\frac{\partial u}{\partial \tilde{x}} - \overline{u\frac{\partial u}{\partial \tilde{x}}}^{\tilde{y}}\right) + \left(v'\frac{\partial u'}{\partial \tilde{y}} - \overline{v'\frac{\partial u'}{\partial \tilde{y}}}^{\tilde{y}}\right) + \left(w\frac{\partial u}{\partial z} - \overline{w\frac{\partial u}{\partial z}}^{\tilde{y}}\right)}_{\mathrm{AA'}_{\tilde{x}}} = \underbrace{-\frac{1}{\rho}\frac{\partial P'}{\partial \tilde{x}}}_{\mathrm{PG'}_{\tilde{x}}} + \underbrace{fv'}_{\mathrm{CA'}_{\tilde{x}}} + \frac{\partial}{\partial z}\underbrace{\left(A_\nu\frac{\partial u}{\partial z} - \overline{A_\nu\frac{\partial u}{\partial z}}^{\tilde{y}}\right)}_{\mathrm{VM'}_{\tilde{x}}} \tag{7a}$$

$$\underbrace{\frac{\partial v'}{\partial t} + \overline{v}^{\tilde{y}}\left(\frac{\partial v'}{\partial \tilde{y}} - \overline{\frac{\partial v'}{\partial \tilde{y}}}^{\tilde{y}}\right)}_{\mathrm{LA'}_{\tilde{y}}} + \underbrace{\left(u\frac{\partial v}{\partial \tilde{x}} - \overline{u\frac{\partial v}{\partial \tilde{x}}}^{\tilde{y}}\right) + \left(v'\frac{\partial v'}{\partial \tilde{y}} - \overline{v'\frac{\partial v'}{\partial \tilde{y}}}^{\tilde{y}}\right) + \left(w\frac{\partial v}{\partial z} - \overline{w\frac{\partial v}{\partial z}}^{\tilde{y}}\right)}_{\mathrm{AA'}_{\tilde{y}}} = \underbrace{-\frac{1}{\rho}\left(\frac{\partial P'}{\partial \tilde{y}} - \overline{\frac{\partial P'}{\partial \tilde{y}}}^{\tilde{y}}\right)}_{\mathrm{PG'}_{\tilde{y}}} \underbrace{-fu'}_{\mathrm{CA'}_{\tilde{y}}} + \frac{\partial}{\partial z}\underbrace{\left(A_\nu\frac{\partial v}{\partial z} - \overline{A_\nu\frac{\partial v}{\partial z}}^{\tilde{y}}\right)}_{\mathrm{VM'}_{\tilde{y}}} \tag{7b}$$

where the perturbation local acceleration $(\mathrm{LA'}_{\tilde{x}}, \mathrm{LA'}_{\tilde{y}})$ incorporates the cross-front mean advection and represents the local acceleration of (u', v') in a coordinate system moving with $\overline{v}^{\tilde{y}}$. The second term on the LHS denotes perturbation advective acceleration $(\mathrm{AA}'_{\tilde{x}}, \mathrm{AA}'_{\tilde{y}})$. The three perturbation terms on the RHS are the pressure gradient $(\mathrm{PG}'_{\tilde{x}}, \mathrm{PG}'_{\tilde{y}})$, Coriolis forcing $(\mathrm{CA}'_{\tilde{x}}, \mathrm{CA}'_{\tilde{y}})$ and vertical mixing $(\mathrm{VM}'_{\tilde{x}}, \mathrm{VM}'_{\tilde{y}})$, respectively. The ensemble and along-front mean of each term in Eq. (7) is estimated (Fig. 14 and Fig. 15). To facilitate the comparison with the TTW and DF mechanisms, we decompose $\mathrm{CA}'_{\tilde{x}}$ into a geostrophic component fv'_{g} that equals to $-\mathrm{PG}'_{\tilde{x}}$, and an ageostrophic component fv'_{a} that equals to $(\mathrm{CA}'_{\tilde{x}} + \mathrm{PG}'_{\tilde{x}})$. As the frontogenesis tendency is mostly within $-1 < \tilde{y} < 0.5\,\mathrm{m}$ (Fig. 13) and $\partial\overline{\langle \rho' \rangle}^{\tilde{x}}/\partial\tilde{y}$ is much stronger over the upper $5\,\mathrm{m}$ (Fig. 12c), the following diagnostics emphasize the results within this $\tilde{y}$ and z range. The ensemble mean momentum balance terms are representative of the momentum terms from the individual test fronts. Also, note that the ensemble mean momentum balance does not reveal what terms were important at times prior or after identification of a test front.

For the along-front momentum terms in Eq. (7a), the perturbation Coriolis forcing $\overline{\langle \mathrm{CA}'_{\tilde{x}} \rangle}^{\tilde{x}}$ (Fig. 14a) is the scaled $\overline{\langle v' \rangle}^{\tilde{x}}$ by definition (Fig. 12e). The perturbation along-front pressure gradient $\overline{\langle \mathrm{PG}'_{\tilde{x}} \rangle}^{\tilde{x}}$ (or $-f\overline{\langle v'_{\mathrm{g}} \rangle}^{\tilde{x}}$) is mostly barotropic (Fig. 14b) and increases northward as indicated from the $\langle \eta' \rangle$ field (Fig. 11a). The corresponding geostrophic component $\overline{\langle v'_{\mathrm{g}} \rangle}^{\tilde{x}}$ decreases northward and $\partial\overline{\langle v'_{\mathrm{g}} \rangle}^{\tilde{x}}/\partial\tilde{y}$ is largely spatially uniform, having a spatial mean (± std) of $-0.22f(\pm 0.11f)$ near the front axis ($-1 < \tilde{y} < 0.5$ km). The ageostrophic Coriolis forcing $(\overline{\langle \mathrm{PG}'_{\tilde{x}} \rangle}^{\tilde{x}} + \overline{\langle \mathrm{CA}'_{\tilde{x}} \rangle}^{\tilde{x}})$ (or $f\overline{\langle v'_{\mathrm{a}} \rangle}^{\tilde{x}}$) is an important contributor to the momentum budget within the upper 5 m (Fig. 14c). The convergence $\partial\overline{\langle v'_{\mathrm{a}} \rangle}^{\tilde{x}}/\partial\tilde{y}$ is primarily concentrated around the front axis. Within the upper 5 m and $-1 < \tilde{y} < 0.5\,\mathrm{km}$, the spatial mean $\partial\overline{\langle v'_{\mathrm{a}} \rangle}^{\tilde{x}}/\partial\tilde{y} = -0.17f$ is comparable to the mean $\partial\overline{\langle v'_{\mathrm{g}} \rangle}^{\tilde{x}}/\partial\tilde{y} = -0.22f$. Thus, both $\overline{\langle v'_{\mathrm{a}} \rangle}^{\tilde{x}}$ and $\overline{\langle v'_{\mathrm{g}} \rangle}^{\tilde{x}}$ are important contributors to the positive straining deformation $\langle F_v \rangle$ around the front axis (Fig. 13b). The ageostrophic Coriolis forcing $f\overline{\langle v'_{\mathrm{a}} \rangle}^{\tilde{x}}$ (or $\overline{\langle \mathrm{PG}'_{\tilde{x}} \rangle}^{\tilde{x}} + \overline{\langle \mathrm{CA}'_{\tilde{x}} \rangle}^{\tilde{x}}$, Fig. 14c) is nearly entirely balanced by the sum of the perturbation local and advective accelerations $(\overline{\langle \mathrm{LA}'_{\tilde{x}} \rangle}^{\tilde{x}} + \overline{\langle \mathrm{AA}'_{\tilde{x}} \rangle}^{\tilde{x}}$, Figs. 14d, e), as the perturbation vertical mixing $\overline{\langle \mathrm{VM}'_{\tilde{x}} \rangle}^{\tilde{x}}$ is small (Fig. 14f). Within the upper $5\,\mathrm{m}$ and $-1 < \tilde{y} < 0.5\,\mathrm{km}$, the spatial rms $\overline{\langle \mathrm{VM}'_{\tilde{x}} \rangle}^{\tilde{x}}$ is $7 - 14\times$ smaller than the rms of the other terms. Within the upper $5\,\mathrm{m}$, $\overline{\langle \mathrm{LA}'_{\tilde{x}} \rangle}^{\tilde{x}}$ is largely positive (negative) on the dense (light) side (Fig. 14d), indicating that the magnitude of the positive (negative) $\overline{\langle u' \rangle}^{\tilde{x}}$ on the dense (light) side (Fig. 12d) increases as the ensemble mean front is strengthening (Fig. 13e). This acceleration is partially driven by $f\overline{\langle v'_{\mathrm{a}} \rangle}^{\tilde{x}}$ (Fig. 14c), with a sign determined by $\overline{\langle \mathrm{CA}'_{\tilde{x}} \rangle}^{\tilde{x}}$ within the upper $5\,\mathrm{m}$ (Fig. 14a). The negligible $\overline{\langle \mathrm{VM}'_{\tilde{x}} \rangle}^{\tilde{x}}$ is different from the TTW balance (McWilliams et al. 2015) and many shallow water bathymetry-forced fronts (*e.g.,* Simpson et al. 1978) . The balance between the perturbation $f\overline{\langle v'_{\mathrm{a}}\rangle}^{\tilde{x}}$ and the perturbation material (local plus advective) acceleration is analogous to the DF along-front balance (Hoskins et al. 1978).

For the cross-front momentum terms, the perturbation $\overline{\langle \mathrm{CA'}_{\tilde{y}}\rangle}^{\tilde{x}}$ (Fig. 15a) reflects a scaled $\overline{\langle u'\rangle}^{\tilde{x}}$ (Fig. 12d). The perturbation cross-front pressure gradient $\overline{\langle \mathrm{PG'}_{\tilde{y}}\rangle}^{\tilde{x}}$ has both barotropic and baroclinic contributions (Fig. 15b). At the front axis, the $\overline{\langle \mathrm{PG'}_{\tilde{y}}\rangle}^{\tilde{x}}$ is negative at surface (directed to the light side, as indicated in Fig. 11a), and increases downward due to the negative cross-front density gradient (Fig. 12c). Clearly $\overline{\langle \mathrm{CA'}_{\tilde{y}}\rangle}^{\tilde{x}}$ and $\overline{\langle \mathrm{PG'}_{\tilde{y}}\rangle}^{\tilde{x}}$ do not balance, and $(\overline{\langle \mathrm{CA'}_{\tilde{y}}\rangle}^{\tilde{x}} + \overline{\langle \mathrm{PG'}_{\tilde{y}}\rangle}^{\tilde{x}})$ (Fig. 15c) is dominated by $\overline{\langle \mathrm{PG'}_{\tilde{y}}\rangle}^{\tilde{x}}$. As in the along-front direction, the cross-front pressure gradient plus Coriolis acceleration is nearly entirely balanced by cross-front material acceleration $(\overline{\langle \mathrm{LA'}_{\tilde{y}}\rangle}^{\tilde{x}} + \overline{\langle \mathrm{AA'}_{\tilde{y}}\rangle}^{\tilde{x}})$, as cross-front perturbation vertical mixing $\overline{\langle \mathrm{VM'}_{\tilde{y}}\rangle}^{\tilde{x}}$ is small (Fig. 15f). Within the upper $5\,\mathrm{m}$ and $-1 < \tilde{y} < 0.5\,\mathrm{km}$, the spatial rms $\overline{\langle \mathrm{VM'}_{\tilde{y}}\rangle}^{\tilde{x}}$ is 7× smaller than the rms of $\overline{\langle \mathrm{PG'}_{\tilde{y}}\rangle}^{\tilde{x}}$ and the negligible perturbation vertical mixing in both directions further supports that the TTW mechanism does not hold here. Within the upper $5\,\mathrm{m}$, the local acceleration $\overline{\langle \mathrm{LA'}_{\tilde{y}}\rangle}^{\tilde{x}}$ is largely negative (positive) on the dense (light) side (Fig. 15d), implying that the magnitude of the positive (negative) $\overline{\langle v'\rangle}^{\tilde{x}}$ on the dense (light) side (Fig. 12e) decreases as the ensemble mean front is strengthening (Fig. 13e). This decrease is partially driven by $\overline{\langle \mathrm{PG'}_{\tilde{y}}\rangle}^{\tilde{x}}$ within the upper $5\,\mathrm{m}$ (Figs. 15b).

Overall, the along- ensemble front ageostrophic balance is analogous to that in the DF mechanism (Hoskins et al. 1978; Thomas et al. 2008). One striking difference is that, the ensemble front is not in cross-front geostrophic balance, whereas the DF mechanism has an approximate cross-front geostrophic balance (*e.g.,* Hoskins and Bretherton 1972). The cross-front momentum balance between $\overline{\langle \mathrm{PG'}_{\tilde{y}}\rangle}^{\tilde{x}}$ and the material (local plus advective) acceleration is analogous to a nonlinear gravity wave (Sutherland 2010), which would have a sense of alongshore propagation. These results indicate that, the ensemble mean cross-shore oriented front is ageostrophic, develops within a strain field, and is bounded by the shoreline (see onshore weakening $\langle u'\rangle$ in Fig. 11d). FIG. 14

FIG. 15

7. Discussion

a. Coastal density front properties

Within the three-month analysis period, the density gradient magnitude and orientation contrast with previous studies. Here, the number of cross-shore fronts (with a ±50° range of θ_{f}), is one third that of alongshore fronts (Fig. 5a and Fig. 6). Even with taking the θ_{f} range into account, this contrasts with previous high (75 m) resolution coastal numerical model results (Dauhajre et al. 2017), where a cross-isobath density gradient was a factor 20 more probable than an along-isobath density gradient in depths ≤ 50 m. Here, the subtidal stratification N^2 is relatively strong at 10^{-4} s^{-2} to 4×10^{-4} s^{-2} (Fig. 2c), consistent with regional observations (*e.g.,* Palacios et al. 2004). Although Dauhajre et al. (2017) do not report N^2, sections through springtime fronts and filaments allow inference of $N^2 \approx 10^{-5}$ s^{-2}, an order of magnitude weaker than the San Diego Bight simulation. The ensemble cross-shore front has cross-front density gradient $\overline{\langle \partial\rho'/\partial\tilde{y} \rangle}^{\tilde{x}} \approx 2 \times 10^{-4}\,\mathrm{kg\,m^{-4}}$ (Fig. 11), roughly $1-4\times$ the modeled cross-front/filament density gradient for example fronts and filaments on the San Pedro shelf region (Dauhajre et al. 2017). These differences may be due to the differences in large scale LV4 meridional density gradient (*e.g.,* Huyer 1983; Wu et al. 2020), the different study season (winter to spring versus summer to fall, here), the different headland-bay geometries (San Pedro region versus San Diego Bight), or the inclusion of surface gravity wave effects here. These model differences may also be due to grid resolution difference (*i.e.,* $75\,\mathrm{m}$ versus $\sim 30\,\mathrm{m}$) as submesoscale processes were better represented for 100 m versus 36 m grid resolution (resulting in shorter particle retentions, Dauhajre et al. 2019).

The horizontal density gradients here also are larger than deeper-water frontal horizontal density gradients of $O(10^{-4})$–$O(10^{-5})\,\mathrm{kg\,m^{-4}}$ observed in the California Current System (CCS, Pallàs-Sanz et al. 2010; Johnson et al. 2020) over scales of 2–5 km. These differences may be due to the background LV4 meridional density gradient, the general shoreward strengthening of surface horizontal density gradients from deep ($> 500\,\mathrm{m}$) water to the shelf (*e.g.,* Dauhajre et al. 2017), and the high (~ 30 m) grid resolution relative to $O(1)$ km in observations.

Divergence and vorticity are also key front parameters. The ensemble cross-shore front has maximum divergence magnitude $|\overline{\langle \delta' \rangle}^{\tilde{x}}|/f \approx 0.8$ similar to the $|\delta|/f \approx 2$ of the example modeled coastal fronts of Dauhajre et al. (2017). It is also similar to the $\delta/f \approx 0.7$ of Johnson et al. (2020) and $|\delta|/f \approx 0.4$ of Pallàs-Sanz et al. (2010) observed in the CCS. However, the ensemble cross-shore front vorticity $|\overline{\langle \zeta' \rangle}^{\tilde{x}}|/f \approx 0.2$ is rather small relative to $|\zeta|/f \approx 3$ of Dauhajre et al. (2017), likely due to front orientation differences (cross-shore here versus alongshore in Dauhajre et al. 2017) and also to smoothing induced by the ensemble. The ensemble cross-shore front vorticity is also weaker than the $|\zeta|/f \approx 0.7$ observed in CCS fronts (Pallàs-Sanz et al. 2010; Johnson et al. 2020). These CCS fronts are not shoreline boundary impacted, and in total this suggests that cross-shore oriented fronts have reduced vorticity (relative to divergence) due to the shoreline boundary limiting along-front velocity.

Spatial distribution of the $N_{\mathrm{f}} = 528$ cross-shore fronts shows a concentration ($\approx 2/3$ of the fronts) to the north of the TJRE mouth (Fig. 6a2), suggesting that the TJRE shoal may be a factor in promoting cross-shore front generation, as V_{SB} is mostly positive (northward directed). The alongshore front occurrence frequency is elevated with onshore directed surface diurnal baroclinic flow $u_{\mathrm{DU}}^{(1)}$ (Fig. 8b). When $u_{\mathrm{DU}}^{(1)}$ is onshore, surface convergence occurs due to the shoreline boundary. For the alongshore fronts, the cross-front density gradient is positive (warmer water offshore) about 2/3 of the time. This suggests that the alongshore fronts are often, but not always, onshore propagating internal near-surface warm bores (*e.g.,* Colosi et al. 2018; McSweeney et al. 2020) transformed from the diurnal internal tides. At this study site, a nonlinear diurnal internal tide was observed to enhance an alongshore tracer front within 1 km of shore (Grimes et al. 2020). This result may be seasonal and depend on the details of the stratification. Additionally, analysis of surface density fronts would obscure near-bed internal cold bores (*e.g.,* Moum et al. 2007; Sinnett et al. 2018).

b. Comparison with the TTW and DF mechanisms

The TTW mechanism has been invoked to explain density filament generation in specific case studies (*e.g.,* Gula et al. 2014; Dauhajre et al. 2017). A case study of two Gulf Stream density filaments showed that ageostrophic Coriolis forcing is balanced by the vertical mixing (Gula et al. 2014). Another case study of two density filaments and fronts in 20–30 m water depth on the shelf with wind stress ~ $0.03\ \mathrm{N\,m^{-2}}$ found that the horizontal flow field is consistent with the TTW dynamics (Dauhajre et al. 2017). This wind stress was roughly a factor $3\times$ stronger than the typical subtidal wind stress ~ $0.01\ \mathrm{N\,m^{-2}}$ in the San Diego Bight simulations, implying wind speeds $1.7\times$ stronger, consistent with regional spring to fall differences (*e.g.,* Winant and Dorman 1997; Dong et al. 2009). These case studies analyzed individual hand-selected filaments, in contrast to the ensemble front that comprises of 86 test fronts.

As the regional winds are relatively weak and the stratification is strong, we examine whether the TTW mechanism is appropriate for the ensemble front. Utilizing the TTW scaling (Eq. 4.5 of McWilliams 2017)

$$v_{\rm ttw} = \frac{A_v g |\partial \rho / \partial y|}{\rho_0 f^2 d} \tag{8}$$

with characteristic ensemble front $|\partial \langle \rho' \rangle / \partial \tilde{y}| = 1.9 \times 10^{-4}\ \mathrm{kg\,m^{-4}}$, vertical thickness $d \approx 10$ m, and characteristic (vertically-averaged over 10 m) model vertical eddy viscosity $A_v = 2 \times 10^{-3}\ \mathrm{m^2\,s^{-1}}$, yields a cross-front ageostrophic velocity of $v_{\rm ttw} = 0.05\ \mathrm{m\,s^{-1}}$, a value somewhat larger than $\langle v' \rangle$, apriori indicating TTW dynamics could be active. However, TTW dynamics do not apply to the ensemble front. The ensemble front shows weak perturbation vertical mixing $\overline{\langle \mathrm{VM'}_{\tilde{x}} \rangle}^{\tilde{x}}$ and $\overline{\langle \mathrm{VM'}_{\tilde{y}} \rangle}^{\tilde{x}}$ (Eq. 7a and Eq.7b, Fig. 14f, Fig. 15f), indicating that the TTW mechanism is not active in the ensemble front. Furthermore, an idealized TTW generated density front consists of an along-front jet in thermal wind balance and a weaker ageostrophic along-front flow $u_{\rm a}$ that is induced by the cross-front vertical mixing and has an extrema at the front (McWilliams 2017). Here $\langle u' \rangle$ is ageostrophic, varies sign across the front, and has no extrema at the front (Fig. 11d). In the TTW mechanism, the vertical shear of the thermal wind balanced along-front jet induces along-front vertical mixing (McWilliams 2017), but generally requires strong vertical mixing (strong wind forcing which is absent here). In the cross-front direction, the ensemble front is not in a thermal-wind balance as in the upper $5\,\mathrm{m}$ and $-1 < \tilde{y} < 0.5\,\mathrm{km}$, rms of $\partial \overline{\langle u' \rangle}^{\tilde{x}} / \partial z \approx 2 \times 10^{-3}\,\mathrm{s^{-1}}$ (Fig. 12d), is about one quarter the rms of $g/(\rho_0 f)(\partial \overline{\langle \rho' \rangle}^{\tilde{x}} / \partial \tilde{y} \approx 8 \times 10^{-3}\,\mathrm{s^{-1}}$, predicted from a thermal wind balance. This weak vertical shear is consistent with the weak vertical mixing of momentum $\overline{\langle \mathrm{VM'}_{\tilde{x}} \rangle}^{\tilde{x}}$ (Fig. 14f).

In the DF mechanism, the large-scale strain field is non-divergent and in geostrophic balance (*e.g.,* Hoskins and Bretherton 1972; McWilliams 2017). Here, $\langle \overline{u}^{\tilde{y}} \rangle$ is divergent and largely in geostrophic balance within $-6 < \tilde{x} < -4$ km (Fig. 10c). The geostrophic component of the perturbation cross-front flow $\overline{\langle v'_{\rm g} \rangle}^{\tilde{x}}$ is largely uniformly convergent over the $(\tilde{y}, z)$ domain (Fig. 14b). Within the upper $10\,\mathrm{m}$ and $-2 < \tilde{y} < 2\,\mathrm{km}$, the mean cross-front convergence $\partial \overline{\langle v'_{\rm g} \rangle}^{\tilde{x}} / \partial \tilde{y} \approx -0.21 f$ (Fig. 14b) is largely balanced by the mean along-front divergence $\partial \langle \overline{u}^{\tilde{y}} \rangle / \partial \tilde{x} \approx 0.25 f$ within the same region (Fig. 10c). Thus, $(\langle \overline{u}^{\tilde{y}} \rangle, \langle v'_{\rm g} \rangle)$ are largely non-divergent and in geostrophic balance, analogous to the large-scale DF strain field. The $\langle v'_{\rm g} \rangle$ convergence may be partially due to the LV4 irregular topography (*i.e.,* curved coast). Flow convergence induced by varying topography (*e.g.,* varying river channel width) has been found important for estuarine frontogenesis (*e.g.,* Geyer and Ralston 2015). Embedded within the DF strain field, the DF-mechanism ASC has a mass balance where the cross-front convergence is balanced by the downwelling (*e.g.,* Hoskins 1982; Thomas et al. 2008). Within the frontogenesis region (*i.e.,* $z > -5\,\mathrm{m}$ and $-1 < \tilde{y} < 0.5\,\mathrm{km}$), the mean ageostrophic cross-front convergence $\partial\overline{\langle v'_{\mathrm{a}}\rangle}^{\tilde{x}}/\partial\tilde{y} \approx -0.17f$ (Fig. 14c) is largely balanced by the mean perturbation vertical divergence $\partial\overline{\langle w'\rangle}^{\tilde{x}}/\partial z \approx 0.10f$ (Fig. 12f). Thus, $(\langle v'_{\mathrm{a}}\rangle, \langle w'\rangle)$ are analogous to the ASC in the DF-mechanism. Despite these similarities in mass conservation, the momentum balances fundamentally differ. The DF-mechanisms ASC is semi-geostrophic with a cross-front geostrophic balance and an along-front ageostrophic balance. However, the ensemble front has an opposite balance: the perturbation cross-front momentum balance is ageostrophic (Fig. 15), whereas the along-front momentum balance is largely geostrophic (Fig. 14).

This difference in DF-mechanism ASC and ensemble cross-shore front perturbation momentum balances may be due to the presence of a shoreline boundary. Coastal circulation also is largely semi-geostrophic (*e.g.,* Allen 1980; Lentz et al. 1999), particularly at subtidal time-scales, with largely geostrophic cross-shore momentum balance and largely ageostrophic alongshore balance as wind forcing and nonlinear advection can become important. For open ocean fronts, the along-front flow is unbounded and the cross-front momentum balance can be consistent with a geostrophic (thermal wind) balance. Here the ensemble cross-shore front is constrained by the shoreline and the associated semi-geostrophic momentum balance becomes more consistent with that of coastal circulation. In the end, cross-front convergence is key across various types of surface density fronts from the unbounded TTW and DF to the shoreline-bounded ensemble cross-shore front here, albeit via different dynamics.

c. The cross-front ageostrophic balance: Relationship to a gravity current

The primary cross-front momentum balance between the perturbation $\overline{\langle \mathrm{PG'}_{\tilde{y}}\rangle}^{\tilde{x}}$ and the material acceleration $\overline{\langle \mathrm{LA'}_{\tilde{y}}\rangle}^{\tilde{x}} + \overline{\langle \mathrm{AA'}_{\tilde{y}}\rangle}^{\tilde{x}}$ (Fig. 15) is that of a nonlinear gravity wave (*e.g.,* Sutherland 2010). In the limit of small $\mathrm{LA'}_{\tilde{y}}$, a $\mathrm{PG'}_{\tilde{y}}$ and $\mathrm{AA'}_{\tilde{y}}$ balance is that of a gravity current (*e.g.,* Benjamin 1968). Here, within $z > -5\,\mathrm{m}$ and $-1 < \tilde{y} < 0.5\,\mathrm{km}$, the rms of $\overline{\langle \mathrm{LA'}_{\tilde{y}}\rangle}^{\tilde{x}}$ ($1.9 \times 10^{-6}\,\mathrm{kg\,m^{-4}}$) and $\overline{\langle \mathrm{AA'}_{\tilde{y}}\rangle}^{\tilde{x}}$ ($1.3 \times 10^{-6}\,\mathrm{kg\,m^{-4}}$) are comparable (Fig. 15), and the ensemble front may propagate as a gravity current or a nonlinear gravity wave. Density fronts propagating as gravity currents have been observed in the open ocean with density difference $\Delta\rho$ of 0.2–$0.5\ \mathrm{kg\,m^{-3}}$ (*e.g.,* Johnson

1996; Warner et al. 2018). The transition from a geostrophically balanced open-ocean front to a gravity current has been modeled with resulting $\Delta\rho$ of 0.1–$0.3\ \mathrm{kg\,m^{-3}}$ (Warner et al. 2018; Pham and Sarkar 2018).

The ensemble cross-shore front has similarities with coastal buoyant plume fronts that typically have order of magnitude larger density gradients (*e.g.,* Lentz et al. 2003). Both are cross-shore oriented, shoreline bounded, and have a cross-front ageostrophic balance. Modeled coastal buoyant plumes with much larger density gradients have gravity current dynamics (*e.g.,* Akan et al. 2018). In Lentz et al. (2003), the observed plume front propagates alongshore from the light towards the dense side with a cross-front density difference $\Delta\rho \approx 3.0\,\mathrm{kg\,m^{-3}}$ over $2\,\mathrm{km}$, and propagation speed reaching $\approx 0.5\,\mathrm{m\,s^{-1}}$. For the ensemble front, cross-front density difference $\Delta\langle\rho'\rangle \approx -0.08\,\mathrm{kg\,m^{-3}}$ over $1\,\mathrm{km}$ (Fig. 11c), $37\times$ weaker than the Lentz et al. (2003) plume front. Assuming that the ensemble front represents a two-layer gravity current in $h = 20$ m depth with a upper (lower) layer depth of $h_1 = 5\,\mathrm{m}$ ($h_2 = 15\,\mathrm{m}$), the corresponding gravity current speed is $-\sqrt{g'h_1h_2/(h_1+h_2)} \sim -0.05\ \mathrm{m\,s^{-1}}$ (*i.e.,* southward). This suggest that the ensemble cross-shore front with its weak density gradient propagates as a southward gravity current embedded within the northward large-scale flow ($\langle V_{\mathrm{SB}}\rangle \approx 0.2\ \mathrm{m\,s^{-1}}$, Fig. 7a, b) and the resulting northward $\langle\overline{v}^{\tilde{y}}\rangle \sim 0.1\ \mathrm{m\,s^{-1}}$ (Fig. 10d) likely reflects the net sum of the northward large-scale advection and southward gravity current propagation.

We next explore why the ensemble cross-shore front (made up of the 86 test fronts) has dynamics similar to a gravity current. Modeled density fronts in geostrophic balance can transform into gravity currents for similar density differences as seen here (Warner et al. 2018; Pham and Sarkar 2018). However, the shoreline boundary constrains the cross-shore flow preventing cross-shore oriented fronts from being in near-geostrophic balance, as suggested by the cross-front momentum balance. Note that alongshore oriented fronts, such as the example close to a headland in Dauhajre et al. (2017), have no such limitation. Near-field river plumes behave like gravity currents but for distances larger than a Rossby deformation radius $L_{\mathrm{R}} = Nh/f$ other dynamics are important. The cross-shore fronts are 7–18 km from the SDB mouth, and using $N^2 = 2\times10^{-4}\ \mathrm{s^{-2}}$ and $h = 25$ m results in $L_{\mathrm{R}} \approx 4.5$ km. This and the lack of relationship between cross-shore frontal occurrence and SDB outflow indicate that the cross-shore fronts are not gravity currents directly forced by the SDB outflow.

The modeled San Diego Bight region has a weak (factor $30\times$ smaller than the ensemble cross-shore front) large-scale alongshore density gradient (W20) due to regional upwelling gradients (*e.g.,* Huyer 1983) and warm water outflow from the SDB. W20 noted that the northward directed subtidal depth-averaged alongshore flow along the ≈ 25 m isobath was convergent with divergence of $\approx -0.05f$, much weaker than the divergence of the ensemble front. However, the divergent northward flow acting on the large scale density gradient was found to enhance root-mean-square alongshore density gradients (W20). Here, the cross-shore front occurrence and elevated density gradients were much more likely for stronger northward subtidal flow (Fig. 8a). This suggests that the cross-shore fronts, whose ensemble had gravity current like dynamics, is generated by the combined convergent northward flow acting on the large scale density field.

8. Summary

Here, we investigate the kinematics and dynamics of the coastal (within $10\,\mathrm{km}$ from shore and $< 30\,\mathrm{m}$ water depth) density fronts, using a high resolution numerical model of the San Diego Bight (W20). Density fronts are first identified using the Canny edge detection algorithm and then categorized into alongshore and cross-shore oriented fronts. Statistics of front properties show that, the cross-shore fronts are about 1/3 as numerous as the alongshore fronts. For both front groups, the mean front length reaches $6-8\,\mathrm{km}$, the along-front averaged surface density gradient varies from $2\times$ to $20\times10^{-4}\,\mathrm{kg\,m^{-4}}$. Most ($\approx 2/3$) alongshore fronts have lighter water offshore, while 90% of cross-shore fronts have lighter water to the north. The alongshore front activity is enhanced by onshore surface diurnal flow, indicating onshore propagating internal warm bores. In contrast, the cross-shore front activity is promoted by northward subtidal alongshore flow.

The cross-shore front dynamics are further examined using a subset of the cross-shore fronts that have a negative cross-front density gradient (lighter water to the north). The density and flow field are decomposed into cross-front mean and perturbation components, and then ensemble averaged to generate an ensemble cross-shore front. The cross-front mean flow is largely in geostrophic balance in the along- and cross-front directions. The ensemble front extends several kilometers from shore with a distinct linear front axis and convergent perturbation cross-front flow within the upper $5\,\mathrm{m}$. The perturbation along-front flow within the upper $5\,\mathrm{m}$ is more offshore (onshore) directed on the light (dense) side and weakens onshore. Downwelling occurs on the front dense side, and weaker upwelling occurs on the light side. The ensemble mean front is frontogenetic as the cross-front convergence dominates over the frontolytic vertical advection. Vertical mixing of momentum is weak, indicating that the turbulence thermal wind mechanism is not active. The perturbation along-front momentum balance is largely geostrophic, while the cross-front balance is between the pressure gradient and the material acceleration, analogous to a gravity current. This contrasts with the cross-front geostrophic and along-front ageostrophic balances in classic deformation frontognesis, but is consistent with shoreline-bounded semi-geostrophic coastal circulation. Given that alongshore nonuniform density and alongshore convergent flows are ubiquitous in coastal waters, shallow cross-shore fronts may also occur at many other locations.

Acknowledgments. This work was supported by the National Science Foundation (OCE-1459389) as part of the Cross-Surfzone/Inner-shelf Dye Exchange (CSIDE) experiment. Additional funding is through the Environmental Protection Agency through the North American Development Bank, however it does not necessarily reflect the policies, actions or positions of the U.S. EPA or NADB. This work used the Extreme Science and Engineering Discovery Environment (XSEDE), which is supported by National Science Foundation (ACI-1548562). The numerical simulations were performed on the comet cluster at the San Diego Super Computer Center through XSEDE allocation TG-OCE180013. NOAA provided the NAM atmospheric forcing fields and the bathymetry. SIO Coastal Data Information Program provided wave forcing. Ganesh Gopalakrishnan and Bruce Cornuelle provided CASE model solutions which are available online (http://ecco.ucsd.edu/case.html). We also appreciate extra support from the Tijuana River National Estuarine Research Reserve and the Southern California Coastal Ocean Observing System. Geno Pawlak, Derek Grimes, Angelica Rodriguez and Nirnimesh Kumar provided useful feedback on this work. We thank two anonymous reviewers for helpful comments that improved this manuscript.

REFERENCES

Akan, Çiğdem., J. C. McWilliams, S. Moghimi, and H. T. Özkan-Haller, 2018: Frontal dynamics at the edge of the columbia river plume. *Ocean Modelling*, **122**, doi:https://doi.org/10.1016/j.ocemod.2017.12.001, 1 – 12.

Allen, J. S., 1980: Models of wind-driven currents on the continental shelf. *Annual Review of Fluid Mechanics*, **12**, doi:10.1146/annurev.fl.12.010180.002133, 389–433.

Austin, J. A., and J. A. Barth, 2002: Variation in the position of the upwelling front on the oregon shelf. *Journal of Geophysical Research: Oceans*, **107**, 1–1.

Austin, J. A., and S. J. Lentz, 2002: The Inner Shelf Response to Wind-Driven Upwelling and Downwelling*. *Journal of Physical Oceanography*, **32**, doi:10.1175/1520-0485(2002)032<2171:TISRTW>2.0.CO;2, 2171–2193.

Banas, N., P. MacCready, and B. Hickey, 2009: The columbia river plume as cross-shelf exporter and along-coast barrier. *Continental Shelf Research*, **29**, doi:https://doi.org/10.1016/j.csr.2008.03.011, 292 – 301, physics of Estuaries and Coastal Seas: Papers from the PECS 2006 Conference.

Barkan, R., M. J. Molemaker, K. Srinivasan, J. C. McWilliams, and E. A. D'Asaro, 2019: The role of horizontal divergence in submesoscale frontogenesis. *Journal of Physical Oceanography*, **49**, 1593–1618.

Benjamin, T. B., 1968: Gravity currents and related phenomena. *Journal of Fluid Mechanics*, **31**, doi:10.1017/S0022112068000133, 209–248.

Bleck, R., R. Onken, and J. Woods, 1988: A two-dimensional model of mesoscale frontogenesis in the ocean. *Quarterly Journal of the Royal Meteorological Society*, **114**, 347–371.

Booij, N., R. C. Ris, and L. H. Holthuijsen, 1999: A third-generation wave model for coastal regions: 1. model description and validation. *Journal of Geophysical Research: Oceans*, **104**, doi:10.1029/98JC02622, 7649–7666.

Brink, K., 1987: Upwelling fronts: implications and unknowns. *South African Journal of Marine Science*, **5**, 3–9.

Callies, J., R. Ferrari, J. M. Klymak, and J. Gula, 2015: Seasonality in submesoscale turbulence. *Nature communications*, **6**, 1–8.

Canny, J., 1986: A computational approach to edge detection. *IEEE Transactions on pattern analysis and machine intelligence*, 679–698.

Castelao, R. M., T. P. Mavor, J. A. Barth, and L. C. Breaker, 2006: Sea surface temperature fronts in the california current system from geostationary satellite observations. *Journal of Geophysical Research: Oceans*, **111**.

Chant, R., 2011: 2.11 - interactions between estuaries and coasts: River plumes – their formation, transport, and dispersal. *Treatise on Estuarine and Coastal Science*, E. Wolanski and D. McLusky, eds., Academic Press, Waltham, doi:https://doi.org/10.1016/B978-0-12-374711-2.00209-6, 213 – 235.

Colosi, J. A., N. Kumar, S. H. Suanda, T. M. Freismuth, and J. H. MacMahan, 2018: Statistics of internal tide bores and internal solitary waves observed on the inner continental shelf off point sal, california. *Journal of Physical Oceanography*, **48**, doi:10.1175/JPO-D-17-0045.1, 123–143.

Connolly, T. P., and A. R. Kirincich, 2019: High-resolution observations of subsurface fronts and alongshore bottom temperature variability over the inner shelf. *Journal of Geophysical Research: Oceans*, **124**, 593–614.

Dauhajre, D. P., J. C. McWilliams, and L. Renault, 2019: Nearshore lagrangian connectivity: Submesoscale influence and resolution sensitivity. *Journal of Geophysical Research: Oceans*, **124**, 5180–5204.

Dauhajre, D. P., J. C. McWilliams, and Y. Uchiyama, 2017: Submesoscale coherent structures on the continental shelf. *Journal of Physical Oceanography*, **47**, 2949–2976.

Dewey, R. K., and J. N. Moum, 1990: Enhancement of fronts by vertical mixing. *Journal of Geophysical Research: Oceans*, **95**, 9433–9445.

Dinniman, M. S., and M. M. Rienecker, 1999: Frontogenesis in the north pacific oceanic frontal zones—a numerical simulation. *Journal of Physical Oceanography*, **29**, doi:10.1175/1520-0485(1999)029<0537:FITNPO>2.0.CO;2, 537–559.

Dong, C., E. Y. Idica, and J. C. McWilliams, 2009: Circulation and multiple-scale variability in the southern california bight. *Progress in Oceanography*, **82**, doi:https://doi.org/10.1016/j.pocean.2009.07.005, 168 – 190.

Feddersen, F., M. Olabarrieta, R. T. Guza, D. Winters, B. Raubenheimer, and S. Elgar, 2016: Observations and modeling of a tidal inlet dye tracer plume. *Journal of Geophysical Research: Oceans*, doi:10.1002/2016JC011922.

Franks, P. J., 1992: Phytoplankton blooms at fronts: patterns, scales, and physical forcing mechanisms. *Reviews in Aquatic Sciences*, **6**, 121–137.

Garrett, C. J. R., and J. Loder, 1981: Dynamical aspects of shallow sea fronts. *Philosophical Transactions of the Royal Society of London. Series A, Mathematical and Physical Sciences*, **302**, 563–581.

Geyer, W. R., and D. K. Ralston, 2015: Estuarine frontogenesis. *Journal of Physical Oceanography*, **45**, doi:10.1175/JPO-D-14-0082.1, 546–561.

Grimes, D. J., F. Feddersen, S. N. Giddings, and G. Pawlak, 2020: Cross-shore deformation of a surfzone-released dye plume by an internal tide on the inner shelf. *Journal of Physical Oceanography*, **50**, 35–54.

Gula, J., M. J. Molemaker, and J. C. McWilliams, 2014: Submesoscale cold filaments in the gulf stream. *Journal of Physical Oceanography*, **44**, 2617–2643.

Hally-Rosendahl, K., F. Feddersen, D. B. Clark, and R. Guza, 2015: Surfzone to inner-shelf exchange estimated from dye tracer balances. *Journal of Geophysical Research: Oceans*, **120**, 6289–6308.

Horner-Devine, A. R., R. D. Hetland, and D. G. MacDonald, 2015: Mixing and transport in coastal river plumes. *Annual Review of Fluid Mechanics*, **47**, 569–594.

Hoskins, B., I. Draghici, and H. Davies, 1978: A new look at the ω-equation. *Quarterly Journal of the Royal Meteorological Society*, **104**, 31–38.

Hoskins, B. J., 1982: The mathematical theory of frontogenesis. *Annual review of fluid mechanics*, **14**, 131–151.

Hoskins, B. J., and F. P. Bretherton, 1972: Atmospheric frontogenesis models: Mathematical formulation and solution. *Journal of the Atmospheric Sciences*, **29**, 11–37.

Huyer, A., 1983: Coastal upwelling in the california current system. *Progress in Oceanography*, **12**, doi:https://doi.org/10.1016/0079-6611(83)90010-1, 259 – 284.

Huzzey, L. M., and J. M. Brubaker, 1988: The formation of longitudinal fronts in a coastal plain estuary. *Journal of Geophysical Research: Oceans*, **93**, doi:10.1029/JC093iC02p01329, 1329–1334.

Johnson, E. S., 1996: A convergent instability wave front in the central tropical pacific. *Deep Sea Research Part II: Topical Studies in Oceanography*, **43**, 753–778.

Johnson, L., C. M. Lee, E. A. D'Asaro, L. Thomas, and A. Shcherbina, 2020: Restratification at a california current upwelling front. part i: Observations. *Journal of Physical Oceanography*, **50**, 1455–1472.

Jones, C. T., T. D. Sikora, P. W. Vachon, and J. Wolfe, 2012: Toward automated identification of sea surface temperature front signatures in radarsat-2 images. *Journal of Atmospheric and Oceanic Technology*, **29**, 89–102.

Kahru, M., E. Di Lorenzo, M. Manzano-Sarabia, and B. G. Mitchell, 2012: Spatial and temporal statistics of sea surface temperature and chlorophyll fronts in the california current. *Journal of plankton research*, **34**, 749–760.

Kantha, L. H., and C. A. Clayson, 1994: An improved mixed layer model for geophysical applications. *Journal of Geophysical Research: Oceans*, **99**, doi:10.1029/94JC02257, 25235–25266.

Kumar, N., F. Feddersen, Y. Uchiyama, J. McWilliams, and W. OReilly, 2015: Midshelf to surfzone coupled ROMS–SWAN model data comparison of waves, currents, and temperature: Diagnosis of subtidal forcings and response. *Journal of Physical Oceanography*, **45**, doi:10.1175/JPO-D-14-0151.1, 1464–1490.

Kumar, N., S. H. Suanda, J. A. Colosi, K. Haas, E. Di Lorenzo, A. J. Miller, and C. A. Edwards, 2019: Coastal semidiurnal internal tidal incoherence in the santa maria basin, california: Observations and model simulations. *Journal of Geophysical Research: Oceans*, doi:10.1029/2018JC014891.

Kumar, N., G. Voulgaris, J. C. Warner, and M. Olabarrieta, 2012: Implementation of the vortex force formalism in the coupled ocean-atmosphere-wave-sediment transport (coawst) modeling system for inner shelf and surf zone applications. *Ocean Modelling*, **47**, 65 – 95.

Lentz, S., R. T. Guza, S. Elgar, F. Feddersen, and T. H. C. Herbers, 1999: Momentum balances on the north carolina inner shelf. *Journal of Geophysical Research: Oceans*, **104**, doi:10.1029/1999JC900101, 18205–18226.

Lentz, S. J., S. Elgar, and R. Guza, 2003: Observations of the flow field near the nose of a buoyant coastal current. *Journal of physical oceanography*, **33**, 933–943.

Lévy, M., P. J. Franks, and K. S. Smith, 2018: The role of submesoscale currents in structuring marine ecosystems. *Nature communications*, **9**, 4758.

Mahadevan, A., 2016: The impact of submesoscale physics on primary productivity of plankton. *Annual review of marine science*, **8**, 161–184.

Mauzole, Y., H. Torres, and L.-L. Fu, 2020: Patterns and dynamics of sst fronts in the california current system. *Journal of Geophysical Research: Oceans*, **125**.

McSweeney, J. M., J. A. Lerczak, J. A. Barth, J. Becherer, J. A. Colosi, J. A. MacKinnon, J. H. MacMahan, J. N. Moum, S. D. Pierce, and A. F. Waterhouse, 2020: Observations of shoaling nonlinear internal bores across the central california inner shelf. *Journal of Physical Oceanography*, **50**, doi:10.1175/JPO-D-19-0125.1, 111–132.

McWilliams, J. C., 2016: Submesoscale currents in the ocean. *Proceedings of the Royal Society A: Mathematical, Physical and Engineering Sciences*, **472**, 20160117.

— 2017: Submesoscale surface fronts and filaments: secondary circulation, buoyancy flux, and frontogenesis. *Journal of Fluid Mechanics*, **823**, 391–432.

McWilliams, J. C., J. Gula, M. J. Molemaker, L. Renault, and A. F. Shchepetkin, 2015: Filament frontogenesis by boundary layer turbulence. *Journal of Physical Oceanography*, **45**, 1988–2005.

Moum, J. N., J. M. Klymak, J. D. Nash, A. Perlin, and W. D. Smyth, 2007: Energy transport by nonlinear internal waves. *Journal of Physical Oceanography*, **37**, doi:10.1175/JPO3094.1, 1968–1988.

Nagai, T., N. Gruber, H. Frenzel, Z. Lachkar, J. C. McWilliams, and G.-K. Plattner, 2015: Dominant role of eddies and filaments in the offshore transport of carbon and nutrients in the c alifornia c urrent s ystem. *Journal of Geophysical Research: Oceans*, **120**, 5318–5341.

O'Donnell, J., 2010: *The dynamics of estuary plumes and fronts*, Cambridge University Press. doi:10.1017/CBO9780511676567.009, 186–246.

Ohlmann, J., M. Molemaker, B. Baschek, B. Holt, G. Marmorino, and G. Smith, 2017: Drifter observations of submesoscale flow kinematics in the coastal ocean. *Geophysical Research Letters*, **44**, 330–337.

Palacios, D. M., S. J. Bograd, R. Mendelssohn, and F. B. Schwing, 2004: Long-term and seasonal trends in stratification in the california current, 1950–1993. *Journal of Geophysical Research: Oceans*, **109**, doi:10.1029/2004JC002380.

Pallàs-Sanz, E., T. Johnston, and D. Rudnick, 2010: Frontal dynamics in a california current system shallow front: 1. frontal processes and tracer structure. *Journal of Geophysical Research: Oceans*, **115**.

Pham, H. T., and S. Sarkar, 2018: Ageostrophic secondary circulation at a submesoscale front and the formation of gravity currents. *Journal of Physical Oceanography*, **48**, 2507–2529.

Rao, S., J. Pringle, and J. Austin, 2011: Upwelling relaxation and estuarine plumes. *Journal of Geophysical Research: Oceans*, **116**, doi:10.1029/2010JC006739.

Romero, L., D. A. Siegel, J. C. McWilliams, Y. Uchiyama, and C. Jones, 2016: Characterizing storm water dispersion and dilution from small coastal streams. *Journal of Geophysical Research: Oceans*, **121**, 3926–3943.

Romero, L., Y. Uchiyama, J. C. Ohlmann, J. C. McWilliams, and D. A. Siegel, 2013: Simulations of nearshore particle-pair dispersion in southern california. *Journal of physical oceanography*, **43**, 1862–1879.

Shchepetkin, A. F., and J. C. McWilliams, 2005: The regional oceanic modeling system (roms): a split-explicit, free-surface, topography-following-coordinate oceanic model. *Ocean Modelling*, **9**, 347 – 404.

Simpson, J., C. Allen, and N. Morris, 1978: Fronts on the continental shelf. *Journal of Geophysical Research: Oceans*, **83**, 4607–4614.

Sinnett, G., F. Feddersen, A. J. Lucas, G. Pawlak, and E. Terrill, 2018: Observations of nonlinear internal wave run-up to the surfzone. *Journal of Physical Oceanography*, **48**, doi:10.1175/JPO-D-17-0210.1, 531–554.

Spall, M. A., 1995: Frontogenesis, subduction, and cross-front exchange at upper ocean fronts. *Journal of Geophysical Research: Oceans*, **100**, 2543–2557.

Suanda, S. H., F. Feddersen, and N. Kumar, 2017: The effect of barotropic and baroclinic tides on coastal stratification and mixing. *Journal of Geophysical Research: Oceans*, **122**, 10–156.

Sutherland, B. R., 2010: *Internal Gravity Waves*. Cambridge University Press, doi:10.1017/CBO9780511780318.

Thomas, L. N., A. Tandon, and A. Mahadevan, 2008: Submesoscale processes and dynamics. *Washington DC American Geophysical Union Geophysical Monograph Series*, **177**, doi:10.1029/177GM04, 17–38.

Thompson, L., 2000: Ekman layers and two-dimensional frontogenesis in the upper ocean. *Journal of Geophysical Research: Oceans*, **105**, 6437–6451.

Towns, J., T. Cockerill, M. Dahan, I. Foster, K. Gaither, A. Grimshaw, V. Hazlewood, S. Lathrop, D. Lifka, G. D. Peterson, R. Roskies, J. R. Scott, and N. Wilkins-Diehr, 2014: Xsede: Accelerating scientific discovery. *Computing in Science & Engineering*, **16**, doi:10.1109/MCSE.2014.80, 62–74.

Umlauf, L., and H. Burchard, 2003: A generic length-scale equation for geophysical turbulence models. *Journal of Marine Research*, **61**, doi:doi:10.1357/002224003322005087, 235–265.

Warner, J. C., B. Armstrong, R. He, and J. B. Zambon, 2010: Development of a coupled ocean-atmosphere-wave-sediment transport (coawst) modeling system. *Ocean Modelling*, **35**, 230 – 244.

Warner, S. J., R. M. Holmes, E. H. M. Hawkins, M. S. Hoecker-Martínez, A. C. Savage, and J. N. Moum, 2018: Buoyant gravity currents released from tropical instability waves. *Journal of Physical Oceanography*, **48**, 361–382.

Wenegrat, J. O., and M. J. McPhaden, 2016: Wind, waves, and fronts: Frictional effects in a generalized ekman model. *Journal of Physical Oceanography*, **46**, 371–394.

Winant, C. D., and C. E. Dorman, 1997: Seasonal patterns of surface wind stress and heat flux over the southern california bight. *Journal of Geophysical Research: Oceans*, **102**, doi:10.1029/96JC02801, 5641–5653.

Wu, X., F. Feddersen, S. N. Giddings, N. Kumar, and G. Gopalakrishnan, 2020: Mechanisms of mid- to outer-shelf transport of shoreline-released tracers. *Journal of Physical Oceanography*, **50**, doi:10.1175/JPO-D-19-0225.1, 1813–1837.

Figures

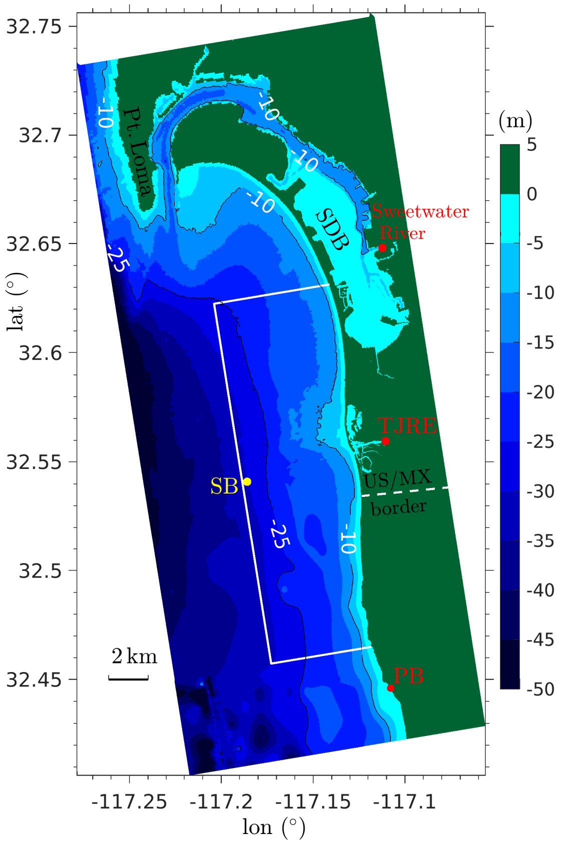

FIG. 1. LV4 grid bathymetry (color shading) and the front study region (white line) to which mean front locations are restricted. Red dots denote the freshwater sources Punta Bandera (PB), Tijuana River estuary (TJRE) and Sweetwater River. The yellow dot denotes the South Bay Ocean Outfall (SB) mooring site in 30 m depth. San Diego Bay (SDB), Point Loma and the US-Mexico border are also labeled.

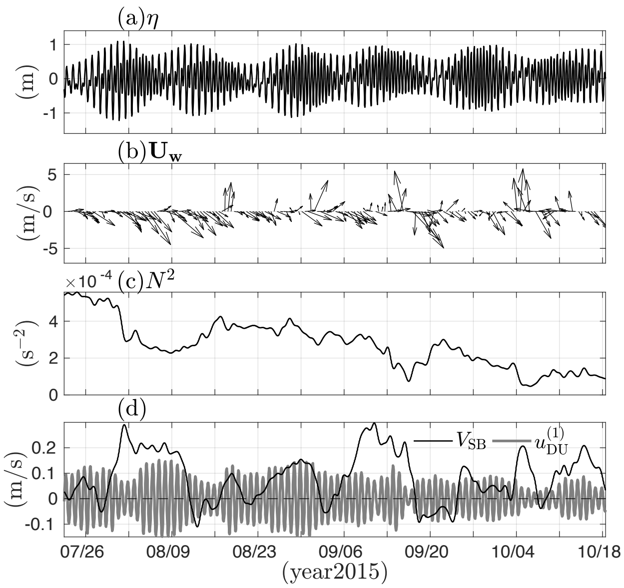

FIG. 2. Time series of (a) sea surface level η at SB, (b) 12 hourly wind vectors at SB, (c) subtidal top-to-bottom buoyancy frequency N^2 at SB, (d) subtidal depth-averaged alongshore velocity at SB $V_{\rm SB}$ and surface cross-shore first-mode diurnal velocity $u_{\rm DU}^{(1)}$ averaged along a smoothed 25 m isobath.

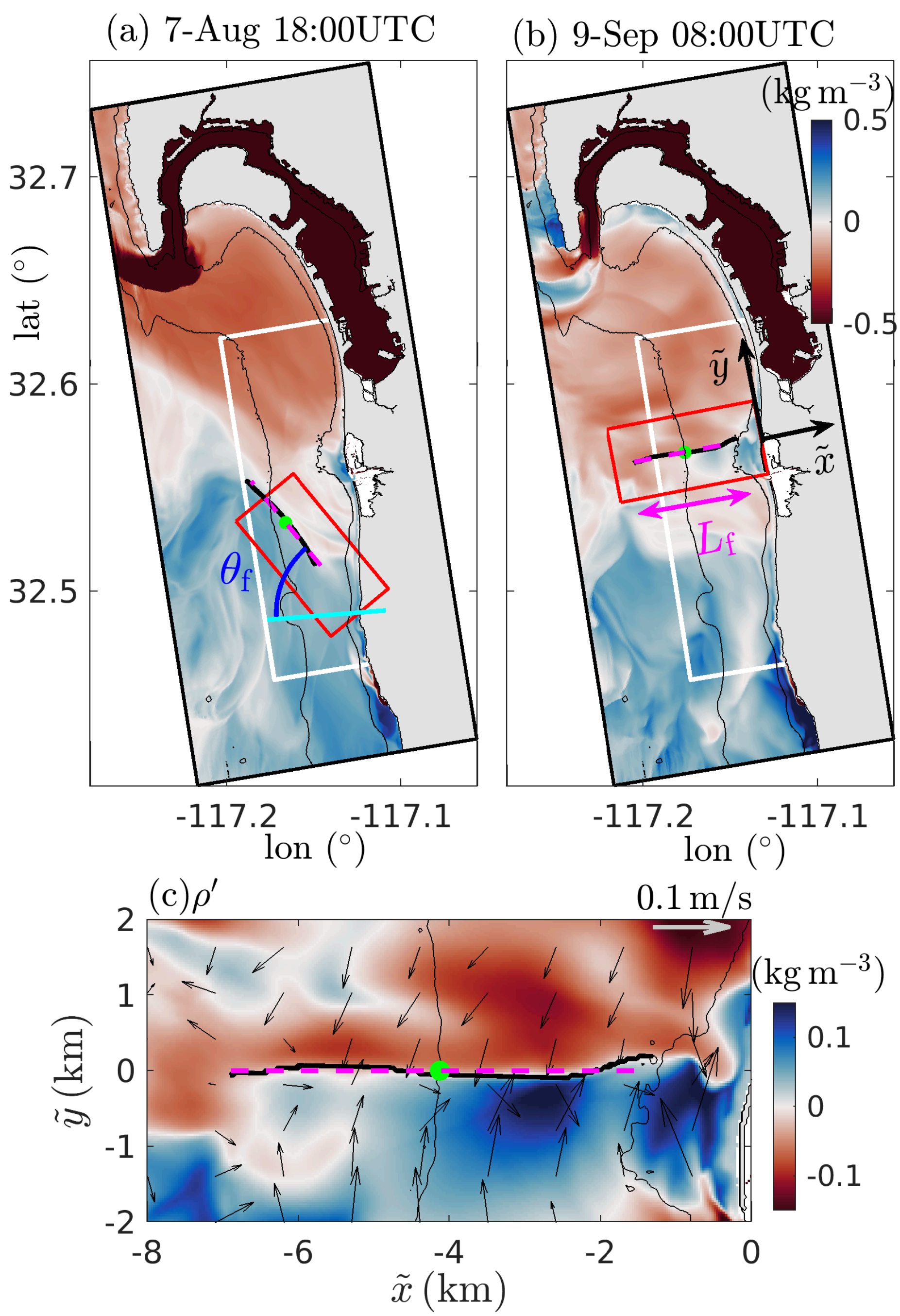

FIG. 3. (top) Surface density perturbation (after removing the spatial mean within the front study region , color shading), the detected front (bold black line) and the frontal control volume (red rectangle) of a (a) inclined and (b) cross-shore oriented front; (c) zoom-in of the cross-shore front density perturbation ρ' (after removing the cross-front mean) and the surface current perturbation (after removing the cross-front mean, vectors) within the control volume in panel (b). In panel (a), the cyan line denotes the shoreline normal direction. In each panel, the green dot shows the mean front location, the dashed magenta line is the front axis, and the thin black contour denotes isobaths $h = [10,\ 25]\,\mathrm{m}$.

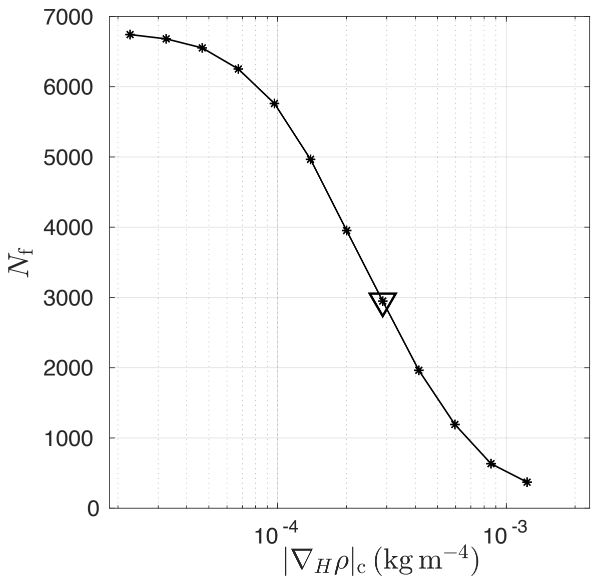

FIG. 4. Total front count N_f versus the cutoff surface density gradient $|\nabla_H \rho|_\mathrm{c}$. The triangle highlights the inflection point of the curve that corresponds to $|\nabla_H \rho|_\mathrm{c}$ = $2.9 \times 10^{-4}\,\mathrm{kg\,m^{-4}}$.

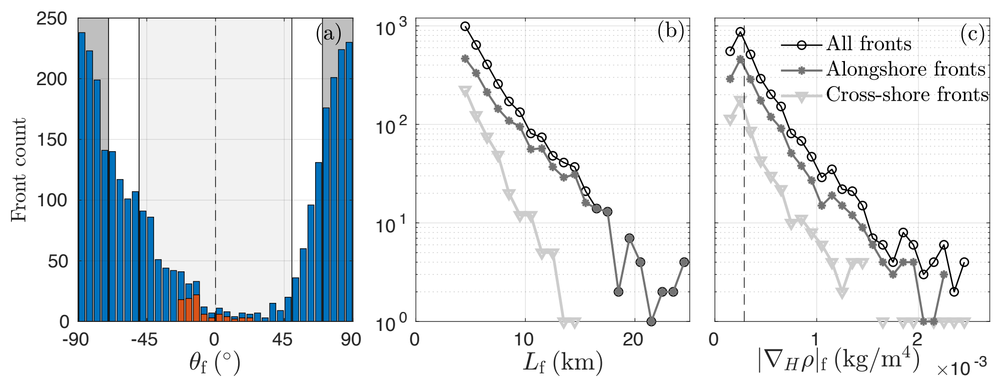

FIG. 5. (a) The front orientation θ_f histogram (blue bars), and histogram (on logarithmic scale) of (b) the front length L_f and (c) the along-front averaged density gradient $|\nabla_H \rho|_\mathrm{f}$ for all the fronts (circle). The fronts are categorized into alongshore (dark gray shading in panel a, star marker in panels b, c), inclined, and cross-shore (light gray shading in panel a, triangle marker in panels b, c). In (a), red histogram indicates the 86 cross-shore fronts used to create the ensemble mean front (Section 4). The dashed line in panel c denotes $|\nabla_H \rho|_\mathrm{c}$.

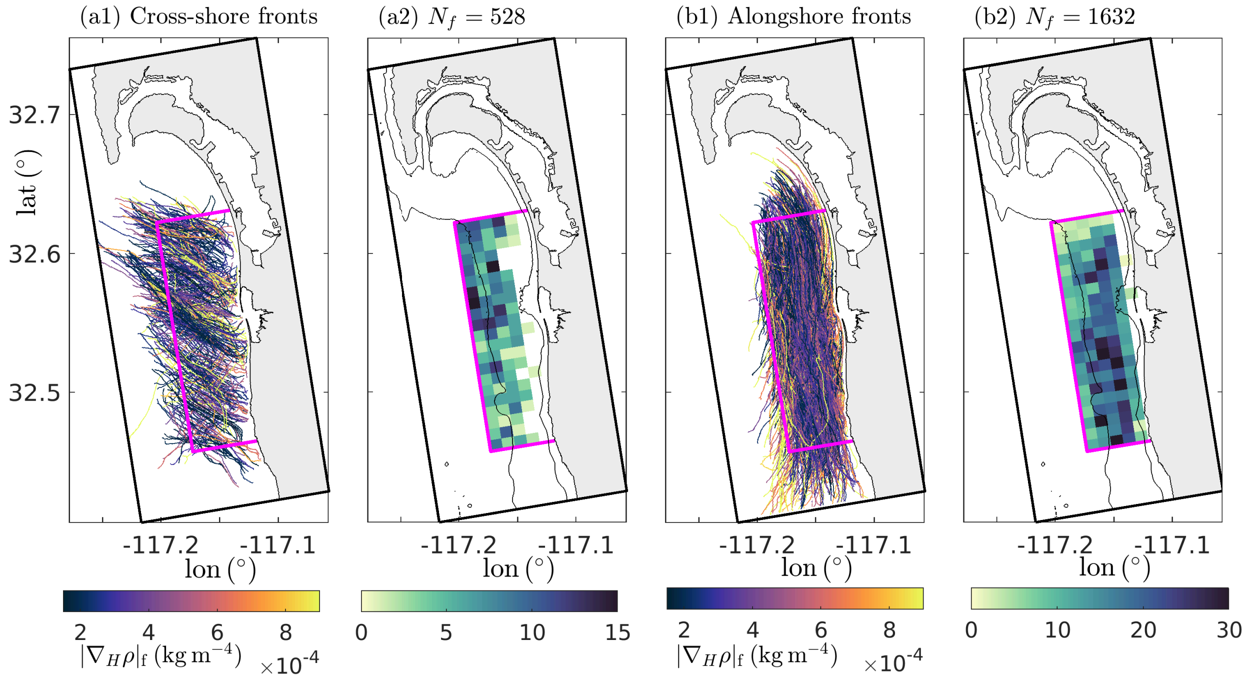

FIG. 6. Front spatial distribution (panels a1 and b1) and the binned mean front location (panels a2 and b2) for all (a) cross-shore and (b) alongshore fronts. In panels a1 and b1, the front color represents the along-front averaged density gradient $|\nabla_H \rho|_f$. Black contours in panels a2 and b2 denote the 10 m and 25 m isobaths.

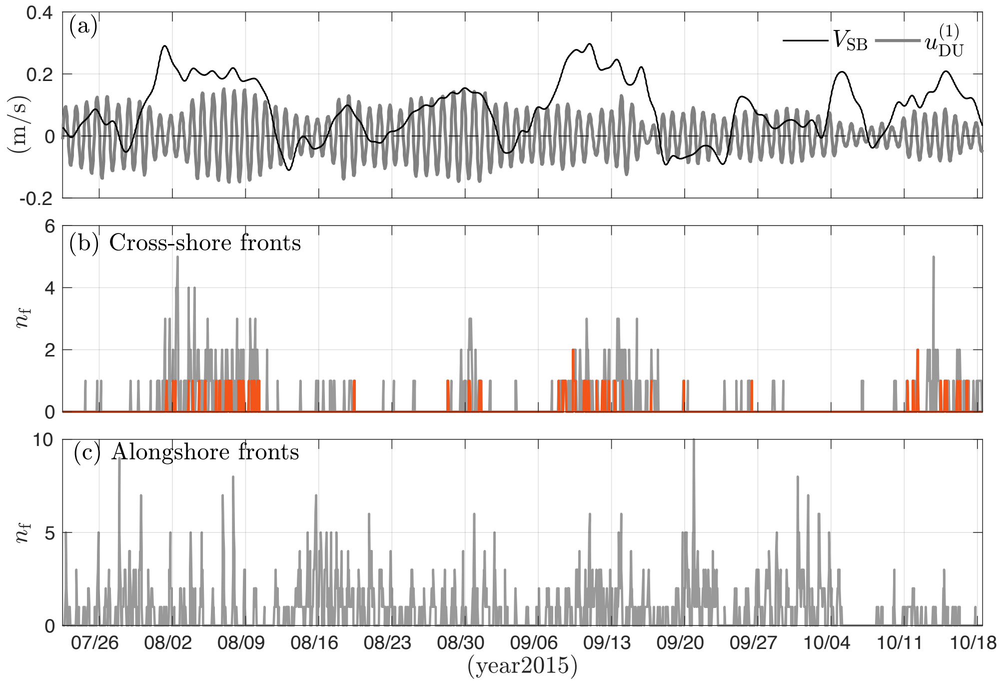

FIG. 7. Time-series of (a) Subtidal alongshore velocity V_{SB} (black) and the diurnal-band surface baroclinic cross-shore velocity $u_{\mathrm{DU}}^{(1)}$ (gray) as in Fig. 2d, (b) hourly front count n_{f} for cross-shore fronts (gray line) and (c) the alongshore fronts. In panel (b) the red line denotes the 86 fronts used to create ensemble mean front (Section 4).

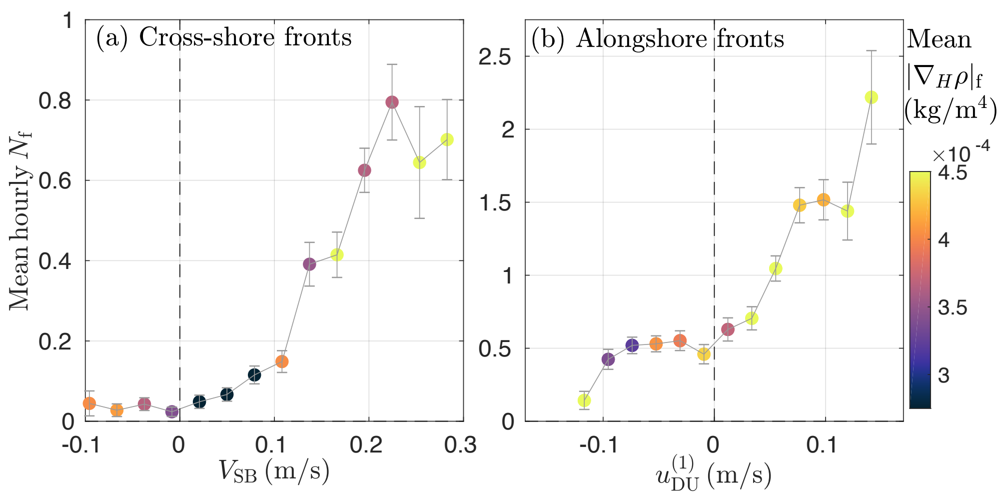

FIG. 8. (a) Bin-averaged hourly front count n_{f} for the cross-shore fronts and the standard error (errorbar) versus the subtidal alongshore velocity at SB V_{SB}. (b) Bin-averaged hourly n_{f} for the alongshore fronts and the standard error (errorbar) versus the diurnal-band first-mode surface cross- shore velocity $u_{\mathrm{DU}}^{(1)}$. In both (a) and (b), the color represents the bin-averaged $|\nabla_H \rho|_{\mathrm{f}}$.

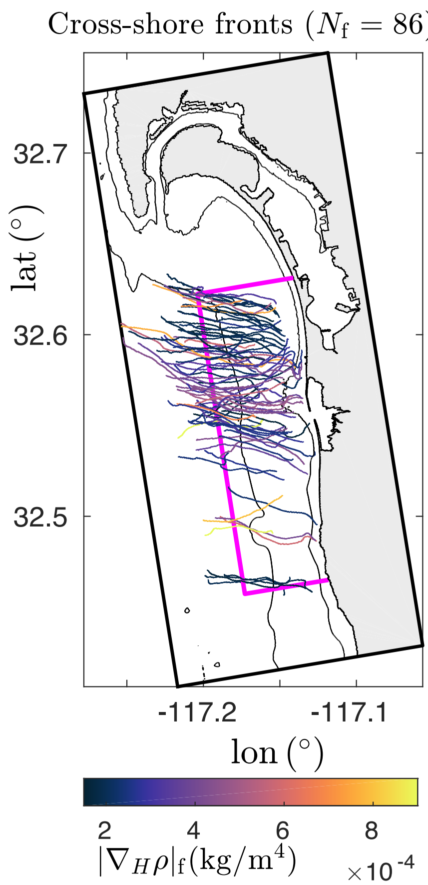

FIG. 9. Spatial distribution of the 86 cross-shore test fronts used to create the ensemble mean front with color representing $|\nabla_H \rho|_{\mathrm{f}}$. Black contours denote the 10 m and 25 m isobaths.

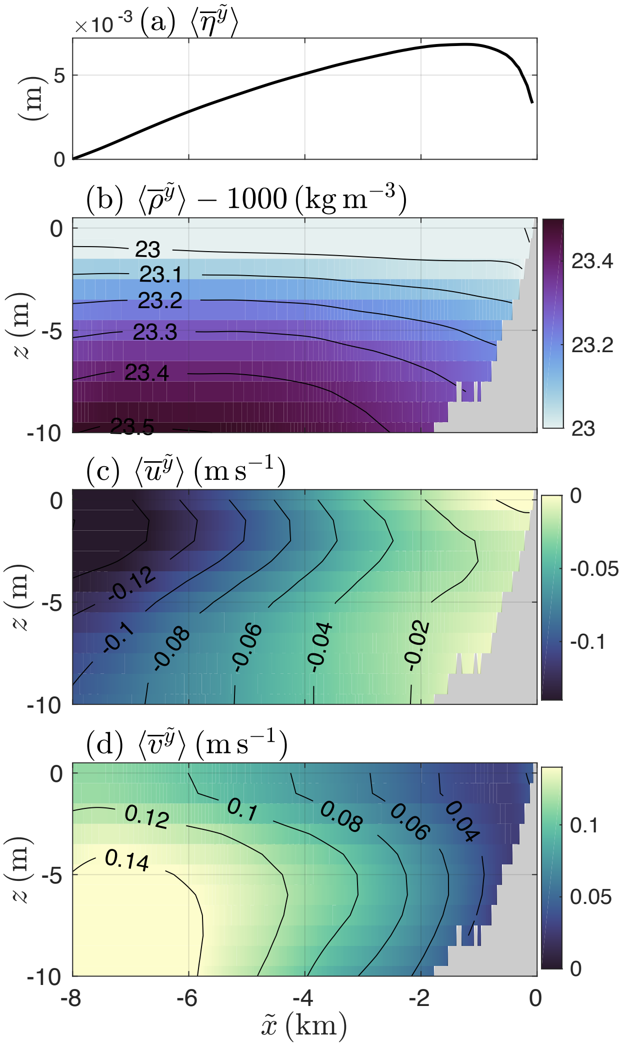

FIG. 10. (a) Ensemble and cross-front averaged sea surface elevation $\langle\overline{\eta}^{\tilde{y}}\rangle$ versus along-front direction $\tilde{x}$. Ensemble and cross-front averaged (b) density anomaly $\langle\overline{\rho}^{\tilde{y}}\rangle - 1000\ \mathrm{kg\,m^{-3}}$, (c) along-front velocity $\langle\overline{u}^{\tilde{y}}\rangle$ and (d) cross-front velocity $\langle\overline{v}^{\tilde{y}}\rangle$ as a function of $\tilde{x}$ and vertical z. Note, the gray shading denotes the cumulative bathymetry from the 86 test fronts.

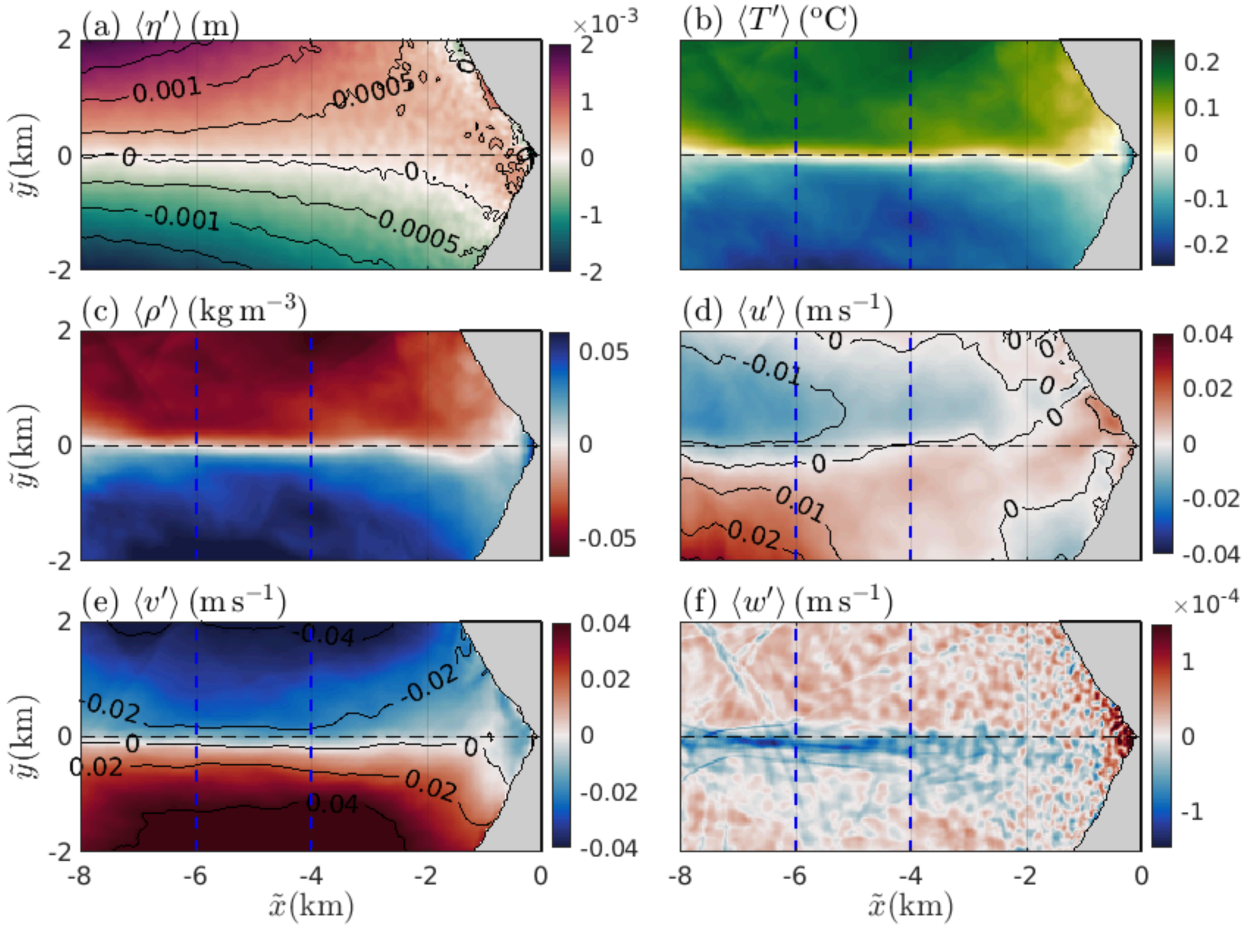

FIG. 11. Plan view of (a) the ensemble perturbation sea surface elevation $\langle \eta' \rangle$, and the near surface (at $z = -1\,\mathrm{m}$) ensemble perturbation (b) temperature $\langle T' \rangle$, (c) density $\langle \rho' \rangle$, (d) along-front velocity $\langle u' \rangle$, (e) cross-front velocity $\langle v' \rangle$, and (f) vertical velocity $\langle w' \rangle$. The blue dashed lines delineate the region ($-6 < \tilde{x} < -4\,\mathrm{km}$) for along-front averaging. The grey shading denotes the cumulative land coverage from the 86 test fronts.

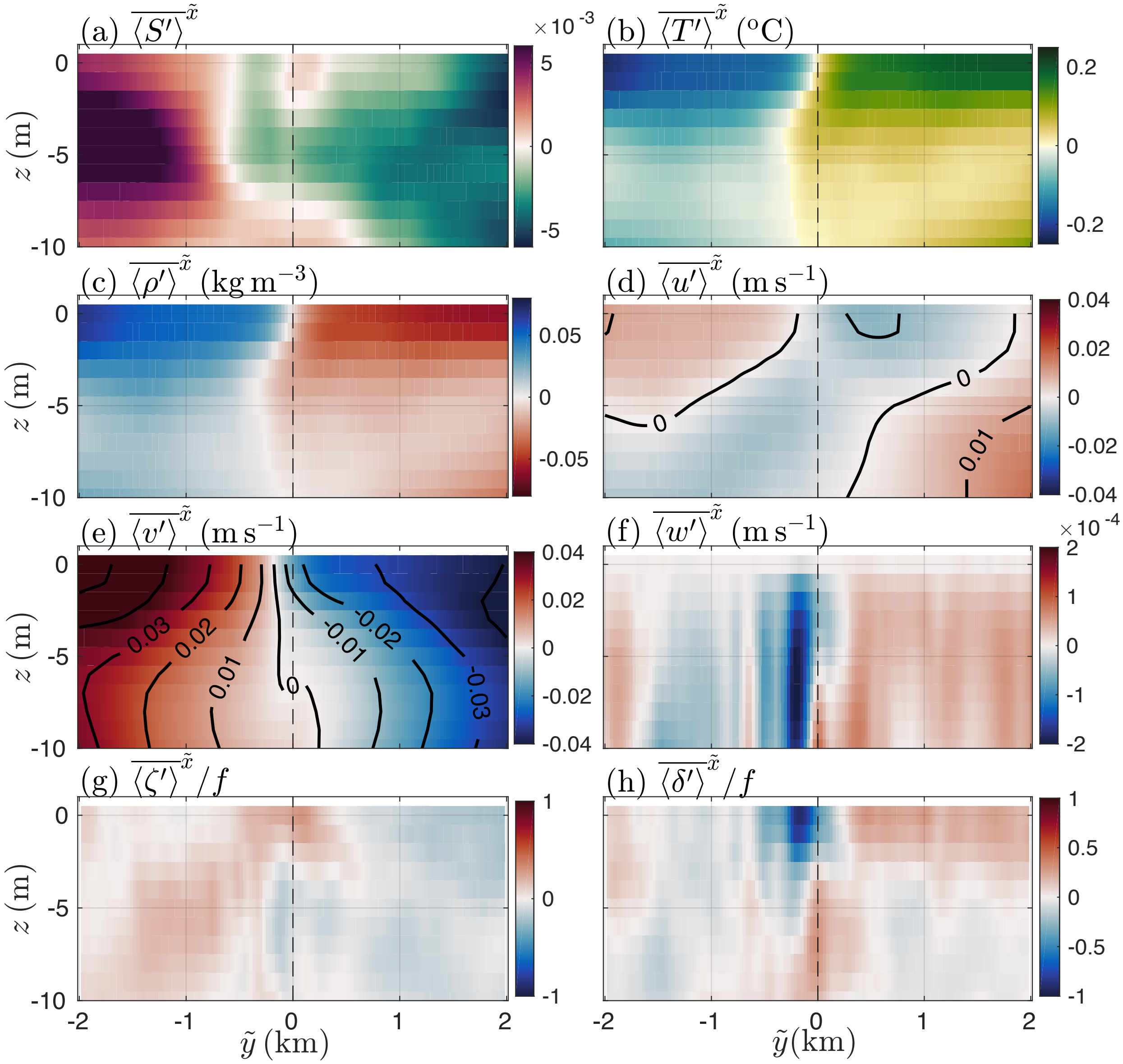

FIG. 12. Ensemble and along-front ($-6 \leq \tilde{x} \leq -4$ km, see blue dashed lines in Fig. 11) averaged perturbation (a) salinity $\overline{\langle S' \rangle}^{\tilde{x}}$, (b) temperature $\overline{\langle T' \rangle}^{\tilde{x}}$, (c) density $\overline{\langle \rho' \rangle}^{\tilde{x}}$, (d) along-front velocity $\overline{\langle u' \rangle}^{\tilde{x}}$, (e) cross-front velocity $\overline{\langle v' \rangle}^{\tilde{x}}$, (f) vertical velocity $\overline{\langle w' \rangle}^{\tilde{x}}$, (g) normalized vertical vorticity $\overline{\langle \zeta' \rangle}^{\tilde{x}}/f$ and (h) normalized divergence $\overline{\langle \delta' \rangle}^{\tilde{x}}/f$ as a function of the cross-front $\tilde{y}$ and vertical z coordinates over the top 10 m of the water column. The black dashed line marks the average front axis ($\tilde{y} = 0$ km). Only the top 10 m is presented as the test fronts minimum water depth at $\tilde{x} = -4$ km is 13 m.

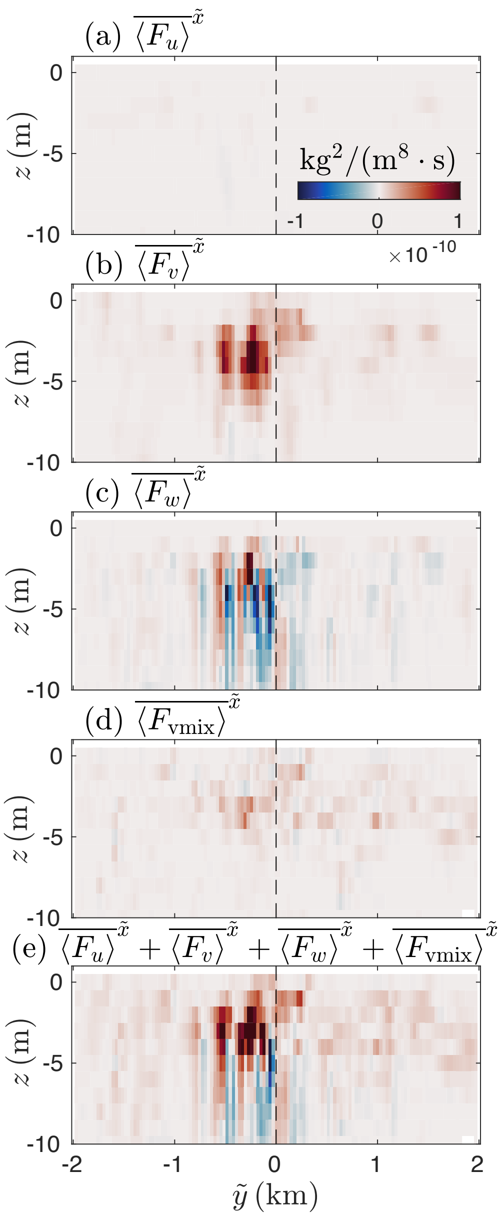

FIG. 13. Ensemble and along-front ($-6 < \tilde{x} < -4\,\mathrm{km}$) averaged frontogenesis tendency terms associated with (a) cross-front shear $\overline{\langle F_u \rangle}^{\tilde{x}}$ (Eq. 6a) (b) cross-front straining $\overline{\langle F_v \rangle}^{\tilde{x}}$ (Eq. 6b), (c) vertical straining $\overline{\langle F_w \rangle}^{\tilde{x}}$ (Eq. 6c), (d) vertical mixing $\overline{\langle F_{\mathrm{vmix}} \rangle}^{\tilde{x}}$ (Eq. 6d), and (e) the total sum as a function of $\tilde{y}$ and z. The black dashed line marks the average front axis.

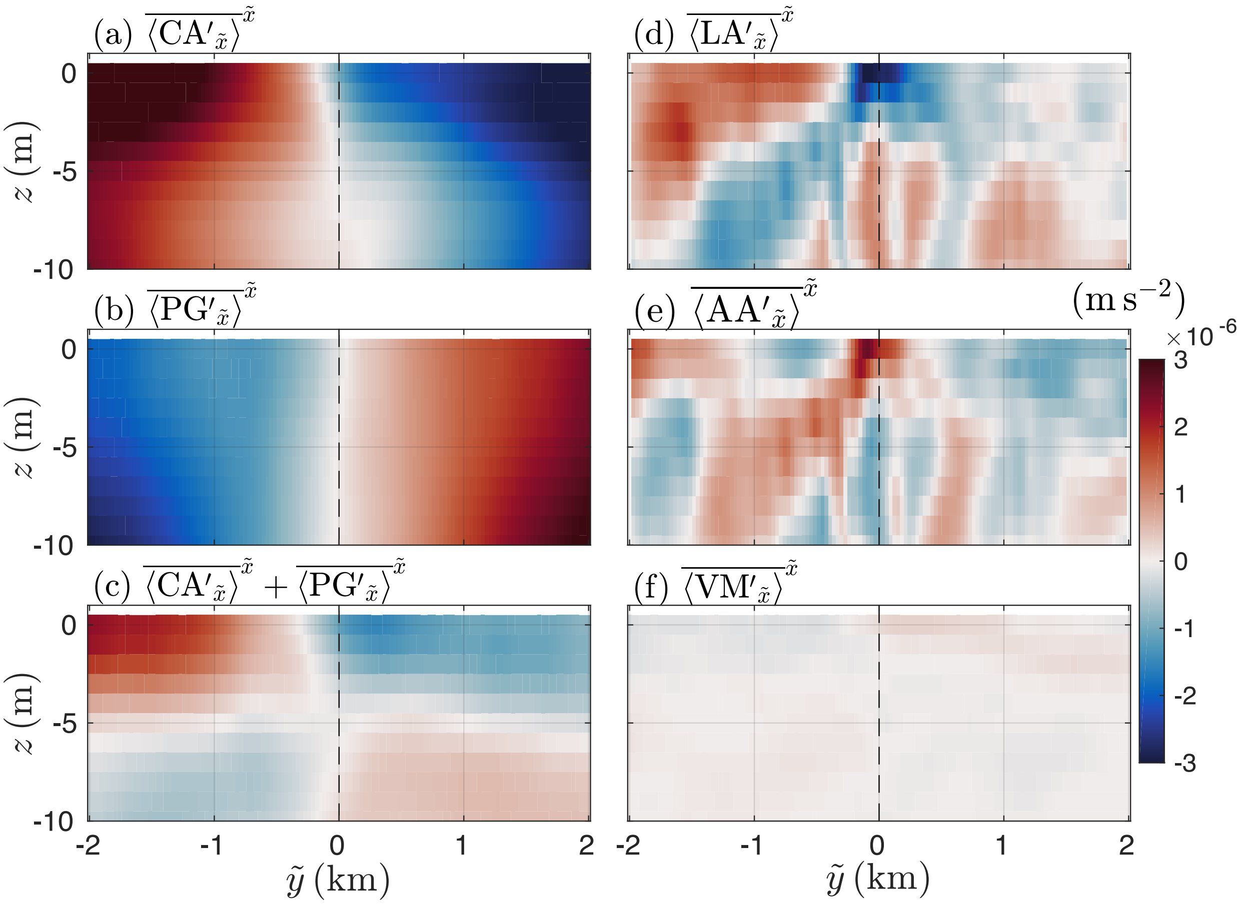

FIG. 14. Ensemble and along-front ($-6 < \tilde{x} < -4\,\mathrm{km}$) averaged perturbation momentum terms in the along-front ($\tilde{x}$) direction: (a) Coriolis forcing $\overline{\langle \mathrm{CA}'_{\tilde{x}} \rangle}^{\tilde{x}}$, (b) pressure gradient $\overline{\langle \mathrm{PG}'_{\tilde{x}} \rangle}^{\tilde{x}}$, (c) ageostrophic Coriolis forcing $\overline{\langle \mathrm{CA}'_{\tilde{x}} \rangle}^{\tilde{x}} + \overline{\langle \mathrm{PG}'_{\tilde{x}} \rangle}^{\tilde{x}}$, (d) local acceleration $\overline{\langle \mathrm{LA}'_{\tilde{x}} \rangle}^{\tilde{x}}$, (e) advective acceleration $\overline{\langle \mathrm{AA}'_{\tilde{x}} \rangle}^{\tilde{x}}$ and (f) vertical mixing $\overline{\langle \mathrm{VM}'_{\tilde{x}} \rangle}^{\tilde{x}}$.

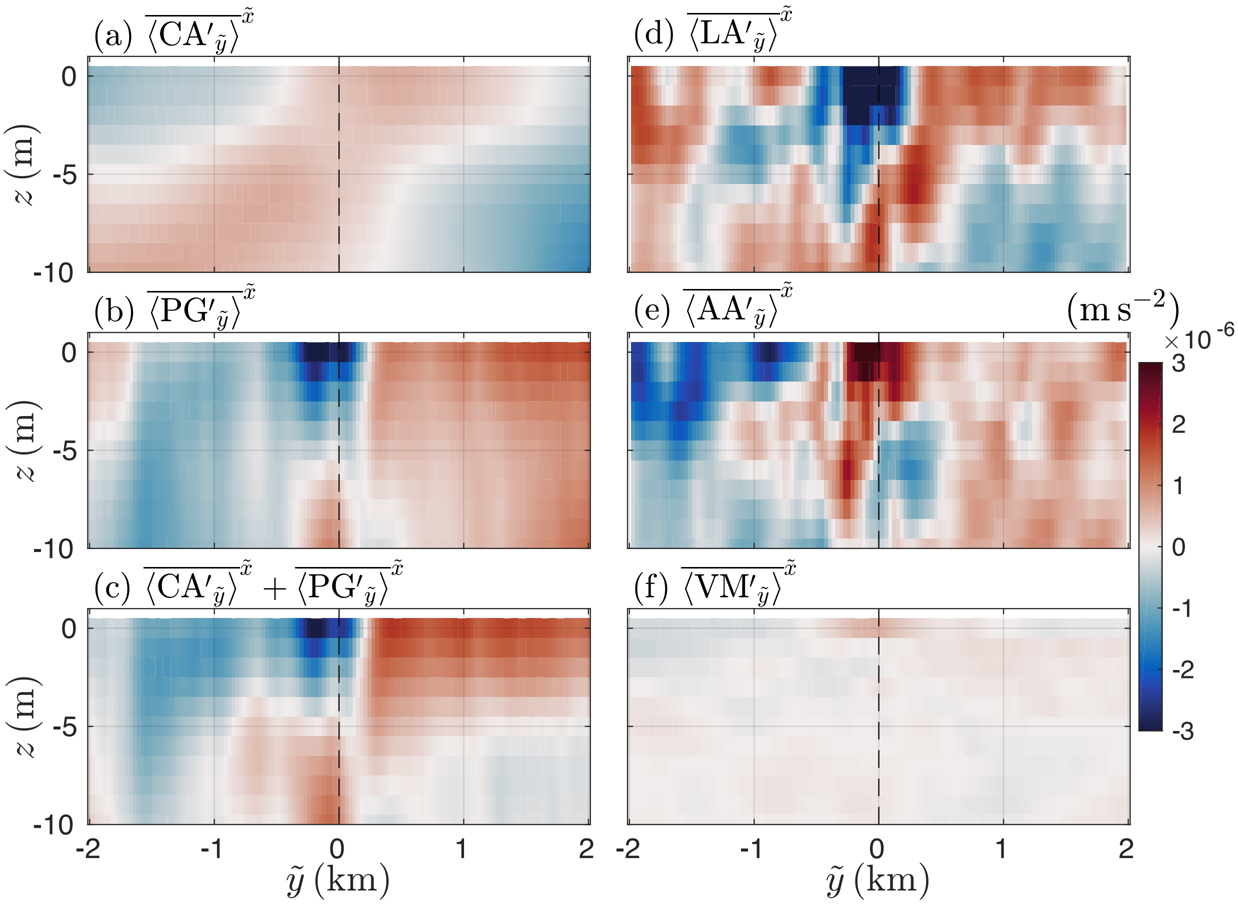

FIG. 15. Similar to Fig. 14 but for the perturbation momentum terms in the cross-front ($\tilde{y}$) direction: (a) Coriolis forcing $\overline{\langle \mathrm{CA}'_{\tilde{y}} \rangle}^{\tilde{x}}$, (b) pressure gradient $\overline{\langle \mathrm{PG}'_{\tilde{y}} \rangle}^{\tilde{x}}$, (c) ageostrophic Coriolis forcing $\overline{\langle \mathrm{CA}'_{\tilde{y}} \rangle}^{\tilde{x}} + \overline{\langle \mathrm{PG}'_{\tilde{y}} \rangle}^{\tilde{x}}$, (d) local acceleration $\overline{\langle \mathrm{LA}'_{\tilde{y}} \rangle}^{\tilde{x}}$, (e) advective acceleration $\overline{\langle \mathrm{AA}'_{\tilde{y}} \rangle}^{\tilde{x}}$ and (f) vertical mixing $\overline{\langle \mathrm{VM}'_{\tilde{y}} \rangle}^{\tilde{x}}$.